ABSTRACT

Title of thesis: EXAMINING THE PASSIVE STIFFNESS WORKSPACE USING VARIABLE STIFFNESS ROBOTS

Evan Feinberg, Masters of Science, 2023

Thesis directed by: Professor David L. Akin
Department of Aerospace Engineering

Passive stiffness control is a method for managing contact forces and dynamics between a robotic manipulator and its environment. Compliance control is typically implemented in redundant serial manipulators using a force torque sensor and active software algorithms. However, time delays in these algorithms can cause large impulse forces between the manipulator and its environment. For applications with limited computation power, large time delays, and low damping, such as In-space Servicing Assembly and Manufacturing (ISAM) and Active Debris Removal (ADR), these effects can cause a manipulator to push away or tip off the target, preventing successful capture.

This thesis examines the implementation of passive stiffness control in a redundant serial manipulator using Variable Stiffness Actuators (VSA). Unlike traditional robot actuators, VSAs have an adjustable stiffness element in series with the primary joint position/control motor to generate varying end-effector position and stiffness. These adjustable springs act as low pass force filters to increase the actuator robustness against external loads at the cost of positioning accuracy. Different optimization algorithms are used to vary the VSA joint stiffness to achieve a desired Cartesian stiffness matrix. However, there are se-

vere limitations with the passive joint to Cartesian stiffness mapping performance over the whole robotic workspace due to the significant kinematic configuration dependence.

Given this limitation, this work attempts to answer for a single, well-defined task, are there regions of the workspace where a prescribed level of passive stiffness realization can be achieved? Or for a mobile robot, can we plan trajectories within a region of the workspace to improve realization performance? This is done by first examining the implementation of three passive stiffness realization methods, each with increasing performance. Next, the idea of Successful Task/Stiffness Trajectories and Success Task/Stiffness Regions are introduced as a way to examine the workspace dependency of the passive stiffness realization. Finally, the application of passive stiffness control for ISAM and ADR applications is studied, and unique design objectives for the manipulator are proposed.

EXAMINING THE PASSIVE STIFFNESS WORKSPACE USING VARIABLE STIFFNESS ROBOTS

by

Evan Feinberg

Thesis submitted to the Faculty of the Graduate School of the
University of Maryland, College Park in partial fulfillment
of the requirements for the degree of
Masters of Science
2023

Advisory Committee:
Professor David L. Akin, Chair/Advisor
Assistant Professor Michael W. Otte
Dr. Craig Carignan

Acknowledgments

I would like to express my appreciation to my thesis supervisor, Dr. David Akin, for his guidance, support, and encouragement throughout the course of my research. I would also like to thank the graduate students within the Space Systems Laboratory, for both helping me navigate the Aerospace Engineering graduate school and for being a sounding board throughout my research. I would like to thank the other members of my thesis committee, Dr. Craig Carignan and Dr. Michael Otte.

Thanks is also due to my colleagues at the U.S. Naval Research Laboratory (NRL). Roxana, Julia, and Joe, your constant advice, technical guidance, and constructive feedback have been instrumental in shaping this thesis and ensuring my success in my research. Steve, thank you for being supportive of losing me for two years while I worked on my research and for enabling me to pursue my passion for developing space robots. Sam, thank you for providing much-needed personal and professional mentorship, and encouraging me to pursue my graduate degree full-time. I would like to acknowledge the financial support provided by the NRL Select Graduate Long-Term Training program. This support has enabled me to further develop my design and analysis skills, which I am excited to bring back to NRL for future program and personal success.

I am indebted to my friends, who have been a constant source of encouragement and support, and who have helped me maintain a healthy work-life balance throughout the course of this project.

And lastly, I want to extend my sincere thanks to my entire family for their unwavering support, encouragement, and belief in me, and for providing me with the inspiration and motivation to pursue my academic goals.

For everyone's invaluable contributions to my professional, academic, and personal journey, thank you again.

Table of Contents

Chapter 1: Introduction

1.1 Motivation and Task Description

With the need for robots to interact with humans and the built environment more closely, the field of soft robotics has exploded to try and meet the challenge. Traditional rigid, redundant manipulators just are not suited for working closely with humans and other sensitive elements of the environment around them. Soft robots often employ compliant materials, deformable bodies, and biomimicry to enable safe interactions with humans or in unknown environments. While this is highly beneficial for disaster response, biomedical applications, or collaborative systems, the increased degrees of freedom and inherent flexibility make soft robots highly difficult to simulate and extremely problematic to control.

Space robots performing In-space Servicing Assembly and Manufacturing (ISAM) and Active Debris Removal (ADR) need to perform a wide range of tasks that result in contradictory requirements on the manipulator. Cutting thermal blankets or unscrewing fill and drain valves [28] requires the manipulator to perform precise positioning and movement. On the contrary, grappling orbital debris and client satellites must be compliant enough to prevent inadvertently translating or rotating away the Resident Space Object (RSO) during grapple [5]. Precise motions require a rigid robot, with minimal backlash and joint and link flexibility, while compliance requires the exact opposite.

Existing space manipulators, such as the Special Purpose Dexterous Manipulator on the International Space Station [11] or the Front-End Robotics Enabling Near-Term Demon-

stration (FREND) arm for the RSGS and OSAM-1 missions [9], can overcome this dichotomy through the use a rigid robot with the addition of a Force Torque Sensor (FTS) and active control algorithms. When compliance is required, such as during grappling or force-limiting tasks, an active impedance control algorithm is used to limit the forces and dynamics imparted on the RSO [20]. However, if the controller time delay becomes large, or the system bandwidth becomes too low, the manipulator cannot regulate the contact forces fast enough [5]. This can be overcome by increasing the system damping, but it results in sluggish behavior of the manipulator. As a result, this behavior can result in the RSO experiencing large impulse forces during capture in addition to shortened contact duration [19] [27], which both can result in the failure to capture the RSO. While significant advances have been made in terrestrial applications for increasing the performance and stability of active impedance control algorithms [11]; constrained onboard computational power, communication delays, and difficulty of testing and validation in a zero-gravity environment limit their application to the space environment [20].

To help alleviate some of the challenges that low system bandwidth causes when capturing an RSO, multiple cooperative grapple interfaces have been designed and proposed which include an additional passive stiffness element. These passive stiffness mechanisms can provide instantaneous compliance due to having zero bandwidth, which can help lower contact forces and increase the duration of contact during a grapple. However, these cooperative servicing interfaces are only designed for a single task and are unable to change their dynamics due to changes in either the client or servicer. The addition of passive compliance has been examined for terrestrial space manipulators, such as the sample transfer arm for the Mars Sample Return mission (MSR). However, the MSR sample transfer arm adds constant passive compliance to the end-effector. However, for grappling existing spacecraft or orbital debris, cooperative grapple interfaces cannot be used, and an alternative method of implementing passive stiffness is needed [20].

Soft robotics is one such method of implementing zero-bandwidth compliance for grappling spacecraft and orbital debris [36]. Soft robots are hyper-redundant robots, typically composed of highly elastic materials, that can mimic biological systems. These robots often use the contraction of these elastic materials to generate motion, often with significantly more degrees of freedom when compared to a rigid robot. During a collision, they can deform and absorb a significant amount of energy. While extremely useful for navigating constrained and constantly changing environments, they are not often suitable for the space environment [26]. This is because most elastic materials, like silicone rubbers, degrade due to the space radiation environment.

One potential method of implementing passive stiffness for the space environment would be using Variable Stiffness Actuators (VSA). A VSA utilizes a variable, passive stiffness element in series with a traditional robot actuator, to enable real-time adjustment of the actuator position and joint stiffness. This results in multiple compelling properties for both terrestrial and space applications including mechanism robustness, increased dynamic performance and energy efficiency, and task adaptability [16].

1.2 Related Work

Human-robot interaction has traditionally been the primary driver of research on serial manipulators with variable, passive joint stiffness. This has led to the development of systems designed to mimic the human arm's ability to perform precise actions while maintaining compliant dynamics. However, given the advancements in the design, simulation, and control of robots utilizing variable stiffness actuators, they are now being considered for tasks within an unknown, unpredictable, or constantly changing environment.

The initial research on robot actuators with passive joint stiffness can be traced to work performed at MIT on Series-Elastic-Elements (SEE) [30]. This involved placing a

spring with constant stiffness in series with a traditional robot actuator. While SEEs implement mechanical robustness into traditional robot manipulators, the constant spring rate forces the manipulator to have a single, kinematic configuration-dependent level of compliance. Early research into designing robot actuators with adjustable joint stiffness was performed initially in Europe thanks to two programs funded by the European Commission. The first was PHRIENDS (Physical human-robot Interaction: dependability and safety) which lasted from 2006 to 2009. The PHRIENDS project made considerable progress with actuator-level modeling and design, with multiple prototype Variable Stiffness Actuators built and tested. This work was further expanded from 2009 to 2012 through the VIACTORS (Variable Impedance ACTuation systems embodying advanced interaction behaviORS) program. Both programs funded research related to variable stiffness robots at multiple universities (University of Pisa, University of Twente, Imperial College London, Italian Institute of Technology, and the Free University of Brussels) as well as the German Aerospace Center (DLR). These programs resulted in the creation of multiple survey papers including a taxonomy of soft robot actuators [39], a detailed description of the relevant actuator properties and parameters in [16], and a detailed guide to the design and trade-offs in [42].

The following sections will attempt to provide a brief overview of current research related to the development and adoption of VSAs. First, advances in actuator design to combine passive stiffness elements in traditional robotic actuators are discussed in subsection 1.2.1. Second, three of the most prominent robots with passive stiffness will be discussed in subsection 1.2.2. Third, an overview of the current state-of-the-art methods for passive stiffness realization is provided in subsection 1.2.3.

1.2.1 Variable Stiffness Actuator Design

There exist many different methods for generating compliance in robotic actuators including pneumatic/hydraulic, electromagnetic/electrostatic, piezoelectric, shape memory alloys, or polymeric actuators [6]. For this thesis, only electro-mechanical systems will be considered given the level of maturity and application to the space environment.

Variable Stiffness Actuators require two separate degrees of freedom, one to change the actuator output position ($\mathbf{q}$) and the second to change the joint mechanical stiffness ($\mathbf{k}_j$). These two requirements can be achieved through different motor configurations and stiffness variation methods. A taxonomy of different VSA types can be found in [39]. Given the specific requirements for ISAM and ADR applications, only the independent VSA and agnostic VSA will be described here. Figure 1.1 provides a diagram describing the two VSA motor arrangements.

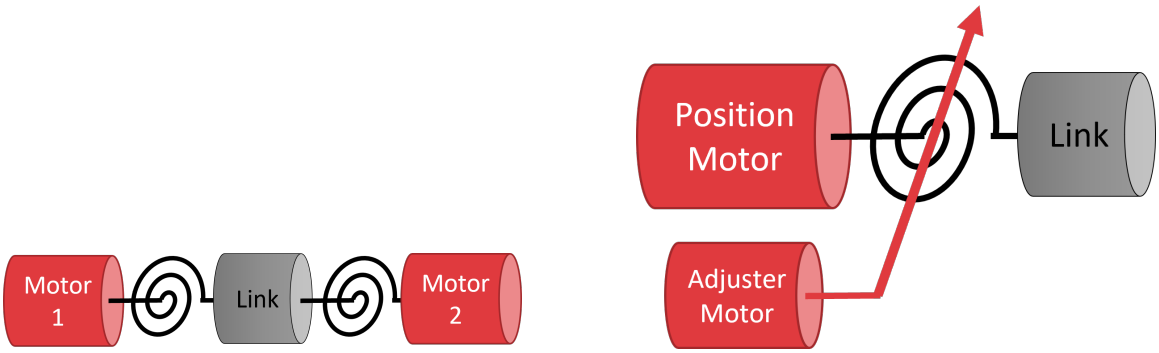

(a) Antagonistic Motors (b) Independent Motors

Figure 1.1: Desired End-Effector Frames on an Inscribed Hemisphere

Designs of antagonistic VSA systems consist of two, customarily identical, motors and springs which oppose one another. Each motor can cause motion by pulling on a joint. The output position is changed by moving both motors in the same direction, while the joint stiffness can be adjusted by moving both motors in opposite directions. This enables

simultaneous adjustment of the output position and stiffness. One benefit to this configuration is that both motors contribute to the change of joint stiffness. However, the maximum output torque and energy storage of the actuator is that of a single motor and spring. Additionally, friction and backlash are caused by both motors and springs. Antagonistic VSAs are commonly designed with tendons functioning as springs, enabling the motors to be placed well inboard of the axis of rotation. This antagonistic behavior directly mimics the muscles in a human arm [21], and thus is often used in humanoid or prosthetic robots.

An early version of an antagonistic VSA was developed by the University of Pisa utilizing an elastic timing belt as a tendon driven by two motors [38]. The timing belt not only transmits torque to the actuator output but also enables variable stiffness by changing the tendon tension. Additionally, the German Aerospace Center developed the Bidirectional Antagonistic Variable Stiffness (BAVS) actuator which uses two motors to adjust a torsional spring to generate variable joint stiffness [14].

Alternatively, independent VSAs separate the two degrees of freedom by having one motor control the output position and a second motor to adjust the torsional stiffness. This is like existing flexible joint robot actuators, where an adjustable torsional spring is placed in series with an existing robot actuator. An independent configuration enables the stiffness adjuster motor to be considerably smaller than the positioning motor. This is because only the positioning motor transmits torque to the actuator output, and the stiffness adjuster only needs to power the stiffness adjuster mechanism. Additionally, energy losses and backlash are typically less for an independent VSA configuration since the adjuster mechanism is not part of the load path. As a result, the independent VSAs are usually lighter than the corresponding antagonistic VSA.

One example of an independent VSA is the Floating Spring Joint (FSJ) developed by the German Aerospace Center. The FSJ was designed to be the first four joints of a humanoid robot arm [40]. The stiffness adjuster mechanism is located on the output side of

the harmonic drive, resulting in larger output inertia. The stiffness adjuster motor rotates two cam disks with respect to each other to stiffen the mechanism. Additionally, the Italian Institute of Technology (IIT) developed the Actuator with Adjustable Stiffness-II (AwAS-II) which utilizes a variable lever arm to adjust the joint stiffness [22]. Interestingly, the range of joint stiffnesses is much greater for such a design ($0-2000Nm/rad$), at the expense of a slower rate of stiffness adjustment. The University of Twente and the University of Bologna co-developed the vsaUT-II [17]. This independent VSA is also able to have an infinite stiffness range by changing the transmission ratio. By moving the application point of the output force on a lever arm, the joint stiffness can be varied from zero to a completely rigid mechanism. Additional examples of both antagonistic and independent VSA designs can be found in the VIACTORS database.

1.2.2 Variable Stiffness Robots

While the research and development of Variable Stiffness Actuators is an active area of research, there has been considerably less effort related to the development of robot manipulators using these actuators. Three of the most prominent passive stiffness robots are Rethink Robotics' Baxter, NASA's Robonaut R2, and the German Aerospace Center's (DLR) Hand-Arm System. Both Baxter and Robonaut use Series Elastic Actuators, while the DLR Hand-Arm System is the only one that actually uses VSAs.

Baxter is an industrial robot, developed by Rethink Robotics, with two 7 Degree-of-Freedom (DoF) arms designed to perform simple manipulation tasks collaboratively with humans [12]. Baxter uses series elastic actuators, with constant passive stiffness and torque sensing, to enable safe operation with humans. The use of series elastic actuators provides a mechanical fail-safe to limit the forces that Baxter can impart on both humans and its environment.

Robonaut R2 was developed in conjunction with NASA Johnson Space Center and General Motors to help assist crew on the International Space Station (ISS) [10]. The anthropomorphic robot was designed to perform maintenance, support astronaut Extra-Vehicular Activity, and provide rapid response to dangerous situations. To enable Robonaut R2 to safely operate in the close presence of astronauts and onboard the ISS, each joint utilizes Series Elastic Actuators to provide shock absorbance and accurate torque control. Robonaut's two 7-DoF arms enable the implementation of fine force sensing/control without impacting the strength or payload capacity. A 12-DoF gripper, where each joint is a tendon-driven variable stiffness actuator, enables Robonaut to dexterously manipulate the same tools as a human.

The DLR Hand-Arm system was designed as a humanoid robot to operate in hard-to-predict environments where environmental collisions are inevitable. As a result, a 7-DoF manipulator, designed to mimic the size, weight, and performance of a human arm was developed [15]. This anthropomorphic arm contains two different types of variable stiffness actuators, which can adjust their joint stiffness during operation to produce desired dynamics for operation. Additionally, a 19-DoF wrist consisting of antagonistic, tendon-driven actuators provides both accurate positioning and stiffness properties. This robot has been used as a testbed to experimentally validate a variety of actuator and arm level control algorithms [4] [29] [41] [24].

1.2.3 Passive Stiffness Realization

The first evaluation of the performance of a non-planar serial manipulator with passive, compliant joints was done by Albu-Schaffer, et. al. [2]. The authors propose a method for determining the optimal joint stiffness values to realize a desired Cartesian stiffness matrix. For a serial manipulator with unconstrained, variable joint stiffness, a method for adjust-

ing the passive stiffness was examined by minimizing a cost function. The performance of Cartesian stiffness realization was shown to have a strong dependence on its kinematic configuration. This results in significant difficulty in achieving an arbitrary Cartesian stiffness matrix throughout the entire robot workspace, even without mechanical joint stiffness limits.

Ott [8] developed a method for exploiting the nullspace motions of a flexible joint, redundant manipulator to map more accurately joint to Cartesian stiffness. While this was initially formulated for lightweight, torque-controlled robots, Petit [13] extended this work for variable stiffness robots and implemented a real-time controller on a 4-DoF variable stiffness robot.

To increase the performance of passive Cartesian stiffness realization, Petit proposed an active Cartesian impedance controller to be used in conjunction with passive realization algorithms in [29] and [13]. A sequential method of first optimizing the passive joint stiffness and then performing an active Cartesian impedance control was able to drastically reduce any realization errors.

Unlike the previously mentioned methods of passive stiffness realization, Rice, et. al., [31] developed an extended inverse kinematics approach to select the joint position and stiffness simultaneously. This was done by augmenting the standard Cartesian and joint configuration vectors with additional compliance terms. While more computationally intensive than previous optimization methods, the extended inverse kinematic approach enables the joint stiffness optimization to be seamlessly integrated with commonly used methods of Cartesian impedance control, singularity detection, and self and environmental collision avoidance.

Despite the strong dependence on kinematic configuration, little work has been done to study the effects of the passive stiffness realization when varying the end-effector's position in the robot workspace. For a planar robot, Petit [13] proposed using stiffability maps

to visualize the optimization performance over the polar reachable workspace. For a planar manipulator with rotational symmetry about its origin, visualization can be simplified to only examine the distance from the end-effector to the origin and the angle between the desired Cartesian stiffness matrix and the origin frame. By generating a series of stiffability maps for different magnitudes of the Cartesian stiffness primary axes, the realization performance can be evaluated across the entire workspace.

While stiffability maps can be a helpful visualization tool for planar robots, such analysis does not easily expand to the non-planar case. Although methods exist for visualizing a robot's reachable [18] and dexterous workspace [43] [9], these visualizations have not been extended for looking at passive stiffness realization performance.

1.3 Problem Statement

One of the fundamental challenges in passive stiffness realization, as was discussed in subsection 1.2.3, is that it is difficult to realize an arbitrary Cartesian stiffness matrix across the entire workspace for a 7-DoF redundant manipulator. This realization gets even worse when one considers the physical limitations such as joint stiffness limits and self-collisions.

For ISAM and ADR applications, robotic servicing vehicles can be specifically designed for a singular task. The robot kinematics, joint stiffness dynamics, and Cartesian stiffness performance can now all be chosen to enable passive stiffness realization for a single use case. This enables the requirement of a variable-stiffness robot to realize an arbitrary Cartesian stiffness to now being restricted to realize a single, well-defined task. Additionally, the requirement for passive stiffness realization over the entire dexterous workspace can now be restricted to a small subset of the workspace. Given these two restrictions, it leads to the following research questions that this thesis will attempt to answer:

1. For a single, well-defined task, are there regions of the workspace where a prescribed level of passive stiffness realization can be achieved?

2. For a mobile robot, can we plan trajectories within a region of the workspace to improve realization performance?

1.4 Thesis Outline

To answer the research questions proposed in this thesis, the properties of an arbitrary variable-stiffness robot will first be examined. The fundamentals of passive stiffness control are studied in detail in chapter 2. Three previously published methods of determining joint stiffnesses given a desired Cartesian stiffness matrix include strictly passive method, a configuration-dependent passive method, and a sequential passive-active method. The implementation and sensitivity to initial conditions provide a detailed explanation for how these passive stiffness control methods could be utilized in practicality.

Once the fundamentals and behavior of a generic robot are well understood, the robot kinematics, joint stiffness dynamics, and desired Cartesian stiffness will be narrowed to attempt to answer the research questions. chapter 3 introduces the specific robot kinematic and VSA joint parameters which are used for future analysis. Additionally, the specific task stiffness and trajectory requirements for ISAM and ADR reference missions will be described in detail.

Next, chapter 4 describes a method for investigating the robot workspace which is commonly used in robot workspace literature. Special attention is paid to the detection and avoidance of kinematic singularities for Candidate Task/Stiffness Trajectories (CTST).

Finally, a detailed examination of the regions of the workspace where a desired performance of passive stiffness control can be ensured is described in chapter 5. The ideas of Successful Task-Stiffness Trajectories (STST) and the Successful Task/Stiffness Region

(STSR) are proposed. A sensitivity analysis is then conducted to evaluate how varying the desired Cartesian stiffness, mechanical joint stiffness limits, and degrees of redundancy affect the number of STSTs and the size and shape of the STSR. This sensitivity analysis is then evaluated with respect to the research questions.

Chapter 2: Passive Stiffness Realization

For redundant manipulators, it is critical to understand the system stiffness in Cartesian space at the end-effector to provide a relationship between the loads imparted by the manipulator onto its environment [25]. If the manipulator has the ability to change its Cartesian stiffness matrix, either through passive or active methods, these values can directly be used to control the contact dynamics of the manipulator. This approach is known as Cartesian impedance control and is a commonly used method for industrial, biomedical, and space applications [39].

While it is desirable to specify a stiffness matrix in Cartesian task space, the physical compliance is generated at each actuator in joint space $\mathbf{q}$. This can be done either through an active joint torque feedback control law or by mechanically changing the joint stiffness properties for variable stiffness robots. As a result, it is of critical importance to have a detailed understanding of the bidirectional stiffness mapping between task and joint space. This will be considered in detail in this chapter.

First, a general robot model and VSA model will be introduced in section 2.1. This thesis examines three different methods for passive stiffness realization to evaluate the performance and limitations of the Cartesian to joint space stiffness mapping. The first, discussed in section 2.4, is a strictly passive method that optimizes the adjustable joint stiffnesses for a given robot configuration. The second, considered in section 2.5, is a configuration-dependent stiffness optimization algorithm that utilizes the nullspace of a redundant manipulator. This finds the optimal joint positions and joint stiffnesses for a

desired end-effector pose and Cartesian stiffness matrix. The last method, described in section 2.6, is a sequential passive-active optimization algorithm that first performs the passive realization to find the optimal joint stiffnesses and then adds an outer-loop active impedance controller to help reduce any outstanding Cartesian stiffness mapping errors. The performance of these three algorithms with respect to their implementation for ISAM and ADR tasks will then be discussed.

2.1 Robot and VSA Model

For a serial manipulator with n rigid joints, an m dimensional motion task can be described in Cartesian space $\mathbf{x} \in \mathbb{R}^m$ at the end-effector. The forward kinematics $\mathbf{f}(\mathbf{q}) : Q \rightarrow X$ describes how the joint positions ($\mathbf{q} \in Q$) can be transformed into a Cartesian end-effector position ($\mathbf{x} \in X$). Additionally, inverse kinematics describes how to find the joint positions for a specified Cartesian position ($\mathbf{q} = f^{-1}(\mathbf{x})$). Joint and Cartesian velocities can be mapped using the kinematic Jacobian $J(\mathbf{q}) = \frac{\partial \mathbf{f}(\mathbf{q})}{\partial \mathbf{x}} \in \mathbb{R}^{m \times n}$. These relationships are summarized by:

$$\mathbf{x} = f(\mathbf{q}) \tag{2.1}$$

$$\dot{\mathbf{x}} = J(\mathbf{q})\dot{\mathbf{q}} \tag{2.2}$$

The forward kinematics will always be able to provide a single Cartesian pose given the joint angles. However, for an under-actuated manipulator ($n \leq m$) there could be no inverse kinematic solution resulting in some Cartesian poses that cannot be achieved by the robot. Additionally, for a redundant manipulator ($n \geq m$) there could be an infinite number of joint configurations to achieve a desired end-effector pose. The method of choosing a

specific joint configuration for a given Cartesian pose is called redundancy resolution and is described in more detail in section 2.5.

For a robot consisting of VSA joints, two additional state variables are needed. This is because the link (or joint) position and the motor (or actuator) position are now no longer the same, and the joint stiffness can be varied. For an independent VSA, each joint now has an actuator position `, link position **q**, and stiffness variation parameter **œ**. These can be seen in Figure 2.1.

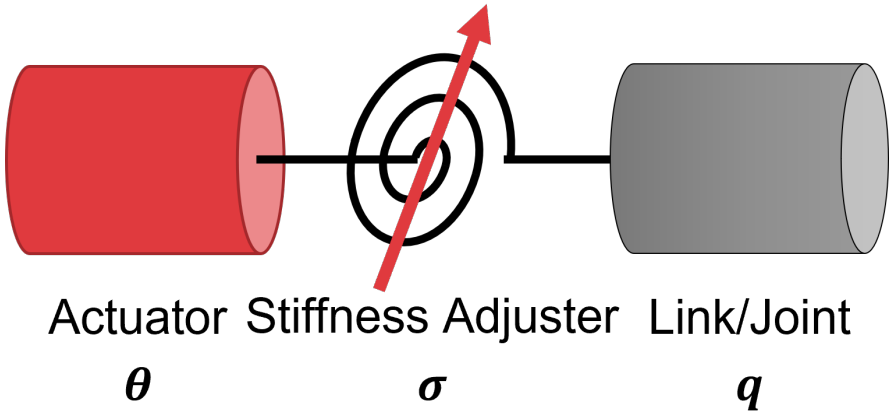

Figure 2.1: State Variables of an Independent Variable Stiffness Actuator

Clearly, the actuator, link, and stiffness variation parameters are all related. The equation of motions which relate the three is defined in [6] and is reproduced below:

$$\begin{bmatrix} m_i & 0 \\ 0 & b_i \end{bmatrix} \begin{bmatrix} \ddot{q}_i \\ \ddot{\theta}_i \end{bmatrix} + \begin{bmatrix} -\tau_i(\phi_i, \sigma_i) \\ \tau_i(\phi_i, \sigma_i) \end{bmatrix} = \begin{bmatrix} \tau_{ext,i} \\ \tau_{m,i} \end{bmatrix} \tag{2.3}$$

$$\tau_i(\phi_i, \sigma_i) = k(f_{cd,i}(\phi_i + \sigma_i) + f_{cd,i}(-\phi_i - \sigma_i))(-j_{1,i} + j_{2,i}) \tag{2.4}$$

One important result of these equations of motion is that for a VSA not at equilibrium (i.e. $\theta_i \neq q_i$), there are an infinite number of combinations of θ_i and σ_i that can result in a

desired link position q_i. This is because if we define the windup of a VSA as $\phi_i = q_i - \theta_i$, the torque within the variable stiffness element is defined as the nonlinear function:

$$\tau = \mathbf{h}(\phi, \sigma) \tag{2.5}$$

This results in the instantaneous joint stiffness of the VSA:

$$\mathbf{k}(\phi, \sigma) = \frac{\partial \mathbf{h}(\phi, \sigma)}{\partial \phi} \tag{2.6}$$

By increasing or decreasing the stiffness variation parameter, the resultant joint stiffness can also be varied. If the flexible joint has a constant stiffness ($k = constant$), as is the case with series elastic actuators, the joint torque becomes $\tau(\phi, \mathbf{k}) = \mathbf{k}\phi$ [41].

There are also inverse functions $\mathbf{h}_{\phi}^{-1}$ and $\mathbf{h}_{\sigma}^{-1}$ to find the required deflection and stiffness parameter for the external resultant actuator torque and link position. Additionally, while the control of a VSA joint is typically done in actuator space θ and stiffness variation space σ, VSA kinematics and trajectories are commonly specified in link space $\mathbf{q}$. This is not only due to the non-uniqueness of ϕ and σ, but also due to the location of mechanical hardstops. VSA typically have mechanical limits on both σ and q, and θ is often unbounded.

For this thesis, it is assumed that the robot level and joint level dynamics will be separated and performed sequentially. First, the passive stiffness control algorithms presented in this thesis will determine the desired link position and joint stiffness for a given Cartesian position and stiffness trajectory. These desired link positions and joint stiffness would then be fed to a VSA joint level controller to find the corresponding θ and σ to follow the link trajectories. This secondary controller will not be considered in this work, given the amount of existing joint-level controller designs [16], and the large dependency on the mechanical design of the actuator.

2.2 Stiffness Mapping

The bidirectional stiffness mapping between joint and Cartesian task space helps in describing a robotic system's response to external loads. This mapping is used heavily in estimating actuator loads given external disturbances [23], traditional active impedance control techniques [35], and also passive stiffness control methods [2]. This mapping and its application to passive stiffness control will be examined in this section.

The Cartesian stiffness matrix K_C relates the Cartesian wrench $\mathbf{f}$ given a Cartesian displacement $\mathbf{x}$. This is given by:

$$K_C = -\frac{\partial \mathbf{f}}{\partial \mathbf{x}} \in \mathbb{R}^{m \times m} \tag{2.7}$$

Alternatively, the joint stiffness matrix K_J relates the joint torque τ given joint position $\mathbf{q}$ given by:

$$K_J = -\frac{\partial \tau}{\partial \mathbf{q}} \in \mathbb{R}^{n \times n} \tag{2.8}$$

Both stiffness matrices are square, with the Cartesian stiffness having a m dimensional task space (typically $m = 6$ for full position and orientation control) and the Joint stiffness having a n dimensional joint space corresponding to the number of joints in the manipulator. The manipulator is said to be redundant if $n > m$, or if there are more joints than the specified task dimensions [37].

The transform from a Cartesian stiffness matrix into a joint stiffness matrix is defined as $\mathscr{T} : K_J = \mathscr{T}(K_C)$. This transform can be computed as:

$$
\begin{aligned}
K_J &= -\frac{\partial \tau}{\partial \mathbf{q}} \\
&= -\frac{\partial (J(\mathbf{q})^\mathsf{T} K_C \Delta \mathbf{x})}{\partial \mathbf{q}} \\
&= J(\mathbf{q})^\mathsf{T} K_C J(\mathbf{q}) - \frac{\partial J(\mathbf{q})^\mathsf{T}}{\partial \mathbf{q}} K_C \Delta \mathbf{x}
\end{aligned} \tag{2.9}
$$

Where $J(\mathbf{q})$ is the manipulator Jacobian ($J(\mathbf{q}) = \frac{\partial \mathbf{f}(\mathbf{q}}{\partial \mathbf{q}}$) and $\Delta\mathbf{x}$ is the Cartesian position error ($\Delta\mathbf{x} = \mathbf{x}_d - \mathbf{x}$). It is common to ignore the position-dependent change of the Jacobian due to analytical complexity [3]. This results in the stiffness being computed about at the equilibrium position, simplifying to:

$$
K_J = J(\mathbf{q})^\mathsf{T} K_C J(\mathbf{q}) \tag{2.10}
$$

This is the basis of early methods for implementing active Cartesian stiffness control [35]. However, this assumption can lead to large errors in the Cartesian stiffness matrix for non-zero position errors, causing K_J and $\mathscr{T}$, to only have local correctness. Enhanced impedance control laws have been investigated by adding the local stiffness correction term [3] at the cost of additional computational time. For this work, Equation 2.10 will be used due to the difficulty of determining $\Delta\mathbf{x}$ online.

To find the Cartesian stiffness matrix from the joint stiffness matrix, one has to solve the inverse of Equation 2.10. This inverse problem is defined as $K_C = \mathscr{T}^{-1}(K_J)$, which is easiest to perform using compliance matrices, ($C_C = K_C^{-1}$, $C_J = K_J^{-1}$) [2]. The inversion is only valid if K_C and K_J are non-singular. K_C and K_J are positive definite matrices for all physical Cartesian and joint stiffness matrices, so the inversion remains valid. Expanding the inversion of Equation 2.9 using the same assumptions of Equation 2.10 gives the

following compliance relationship:

$$C_C = J(\mathbf{q})C_J J(\mathbf{q})^{\mathsf{T}} \tag{2.11}$$

Equivalently, inverting gives the following stiffness relationship:

$$K_C = (J(\mathbf{q}){K_J}^{-1}J(\mathbf{q})^{\mathsf{T}})^{-1} \tag{2.12}$$

One important fact of Equation 2.12 is that to achieve an arbitrary Cartesian stiffness matrix, K_J must be invertible. As long as none of the diagonal elements are zero, i.e. $K_{J(i,i)} = 0$, K_J will be invertible. For a physical system, it is impossible for a diagonal element to have zero stiffness, so the invertibility issue can be ignored.

2.3 Problem Formulation

The problem of finding a joint stiffness matrix that will result in a desired Cartesian stiffness matrix is made difficult due to not having a closed-form solution. This is due to the added restriction of requiring a diagonal joint stiffness matrix. As a result, similar to how inverse kinematics is used to find a series of joint positions to achieve a desired end-effector Cartesian position, one can turn the Cartesian to joint stiffness mapping problem into an optimization problem to find an approximate solution. The problem now becomes:

$$\min_{q,K_{Ja},K_{Jp}} \|K_{Cd} - K_C(\mathbf{q}, K_{Ja}, K_{Jp})\| \tag{2.13}$$

$$s.t. \mathbf{f}(\mathbf{q}) = \mathbf{x_d}$$

$$\mathbf{q}^{min} \leq \mathbf{q} \leq \mathbf{q}^{max}$$

$$K_{Ja}^{min} \leq K_{Ja} \leq K_{Ja}^{max}$$

$$K_{Jp}^{min} \leq K_{Jp} \leq K_{Jp}^{max}$$

Where K_C is the realized Cartesian stiffness matrix due to a given joint stiffness matrix K_J. For strictly passive manipulators, $K_J = K_{Jp}$. However, if a Variable Stiffness Robot has both passive K_{Jp} and active K_{Ja} control, the two are typically added in series. There are some robots that do not have a series interconnection between their passive and active joint stiffness, however, that is relatively uncommon. The series connection between the active and passive joint stiffness can be described as:

$$K_J^{-1} = K_{Ja}^{-1} + K_{Jp}^{-1} \tag{2.14}$$

Equation 2.14 can be simplified by converting the optimization problem into the compliant domain [13]. The goal now is to find the optimal Cartesian compliance matrix C_C, which is a linear combination of the passive Cartesian compliance C_{Cp} and active Cartesian compliance C_{Cp}. The optimization becomes:

$$\min_{q, C_{Ca}, C_{Cp}} \|C_{Cd} - C_C(\mathbf{q}, C_{Ca}, C_{Jp})\| \tag{2.15}$$

$$s.t.\, \mathbf{f}(\mathbf{q}) = \mathbf{x_d}$$

$$\mathbf{q}^{min} \leq \mathbf{q} \leq \mathbf{q}^{max}$$

$$\mathbf{c}_{Jp}^{min} \leq \mathbf{c}_{Jp} \leq \mathbf{c}_{Jp}^{max}$$

This becomes a constrained, nonlinear optimization problem where both the joint positions $\mathbf{q}$ and joint compliance $\mathbf{c}_{Jp}$ need to be examined to find the optimal solution. Special attention also is needed for the minimization norm. [2] considers multiple different norms for optimization including, the induced L2 norm, an intuitive norm based on error qualities, and finally a weighted Frobenius (Schur) norm. The weighted Frobenius norm was chosen given the ability to individually weight each element of the Cartesian stiffness matrix. This allows for the coupling terms, translation/orientation stiffness values, and translation/orientation rotation errors to be weighted separately.

2.4 Passive Joint Compliance Optimization

This section will examine the implementation of Equation 2.15 for a given manipulator configuration ($\mathbf{q}$) and no active compliance ($K_{Ca} = \mathbf{0}$). Two different methods for optimization were examined; a nonlinear solver, and also a linear solver.

2.4.1 Nonlinear Solver

The first method of solving Equation 2.15 was using the built-in Matlab `fmincon` function. `Fmincon` is a constrained, nonlinear solver, able to minimize a cost function according to both a Sequential Quadratic Programming (SQP) and active-set optimization algorithm

subject to linear inequalities. The addition of linear inequalities enables the consideration of mechanical joint stiffness limits in the optimization algorithm.

An evaluation was performed to evaluate the stability and computational time between the two algorithms. For this comparison, first a desired Cartesian stiffness matrix K_{Cd} and end-effector pose $\mathbf{x}$ was selected for all trials. For every trial, a new inverse kinematic solution was performed to find $\mathbf{q}$, and then the passive joint compliance optimizations were computed. The minimized objective function for the given joint configuration $B(\mathbf{q}$ was then computed. The computation time and Compliance mapping norm $B(\mathbf{q}$ is plotted for 1000 trials in Figure 2.2. For each trial, the manipulator configuration is sampled from the redundant nullspace of the manipulator, resulting in different joint configurations. Depending on the initial joint configuration, the passive joint compliance optimization results in different local minima.

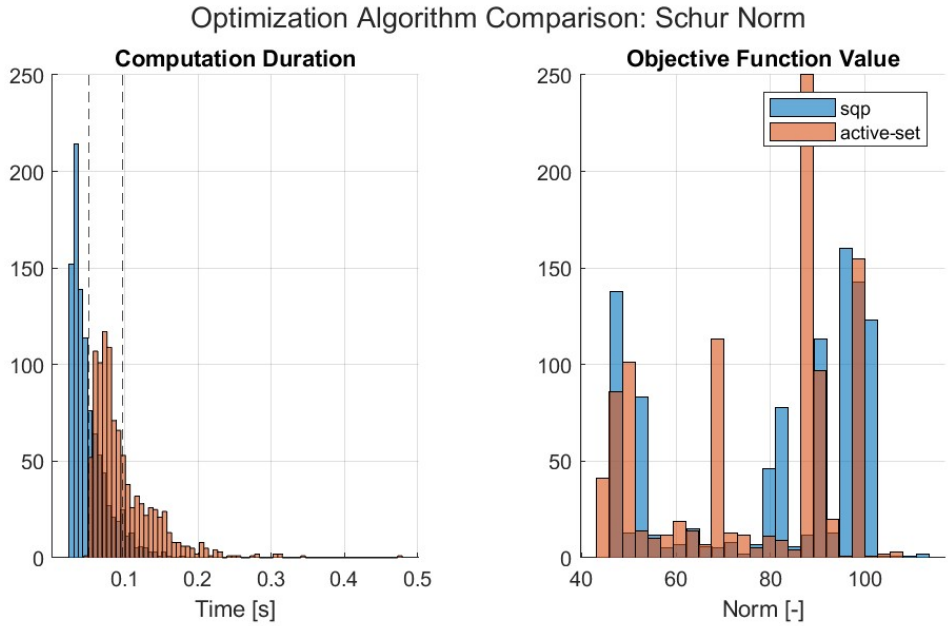

Figure 2.2: Matlab `Fmincon` Algorithm Comparison for a constant desired Cartesian stiffness matrix and end-effector pose

Two different observations can be made from this analysis. The first is for the Matlab

implementation, the SQP algorithm ($\bar{t} = 0.0492s$) is almost 50% faster than the Active-Set algorithm ($\bar{t} = 0.0950s$). The second major observation is the significant configuration dependence on the joint compliance optimization. Selecting a different manipulator configuration could potentially cause the Compliance mapping norm to more than double over the best-case configuration. Exploiting the increased mapping performance depending on the manipulator configuration will be examined in section 2.5.

2.4.2 Linear Solver

To decrease the potential joint compliance optimization computation time, [2] and [29] proposed linearizing the nonlinear formation of Equation 2.15 into a constrained linear least squares form. This is done by first expanding the cost function for joint compliance optimization:

$$\|C_{Cd} - C_{Cp}\|_F^G = \|C_{Cd} - J(\mathbf{q})\mathbf{c}_{Jp}J(\mathbf{q})^\mathsf{T}\|_F^G \tag{2.16}$$

The Frobenius norm can then be rewritten as a Euclidean norm by reshaping both C_{Cd} and C_{Cp} into vectors and differentiating with respect to the passive joint compliance vector $\mathbf{c}_{Jp}$ so that:

$$\begin{aligned}
&\min_{q,c_{Jp}} \|A \cdot \mathbf{c}_{Jp} - \mathbf{b}\|_2^G && (2.17)\\
s.t. \quad & \mathbf{c}_{Jp}^{min} \leq \mathbf{c}_{Jp} \leq \mathbf{c}_{Jp}^{max} \\
where: \quad & A = \frac{\partial}{\partial \mathbf{c}_{Jp}} \left(J(\mathbf{q})\mathbf{c}_{Jp}J(\mathbf{q})^\mathsf{T} \right) \in \mathbb{R}^{m^2 \times n} \\
& \mathbf{c}_{Jp} \in \mathbb{R}^{n \times 1} \\
& \mathbf{b} = \frac{\partial}{\partial \mathbf{c}_{Jp}} C_{Cd} \in \mathbb{R}^{m^2 \times 1}
\end{aligned}$$

An inequality-constrained, linear least-squares solver could then be used to minimize Equation 2.17 subject to the mechanical joint stiffness limits. This was done using the Matlab `lslin` solver. `Lslin` supports both a interior-point-convex and active set algorithm. Similar to the nonlinear case, the two algorithms can be compared to evaluate stability and computation time. This can be seen in Figure 2.3.

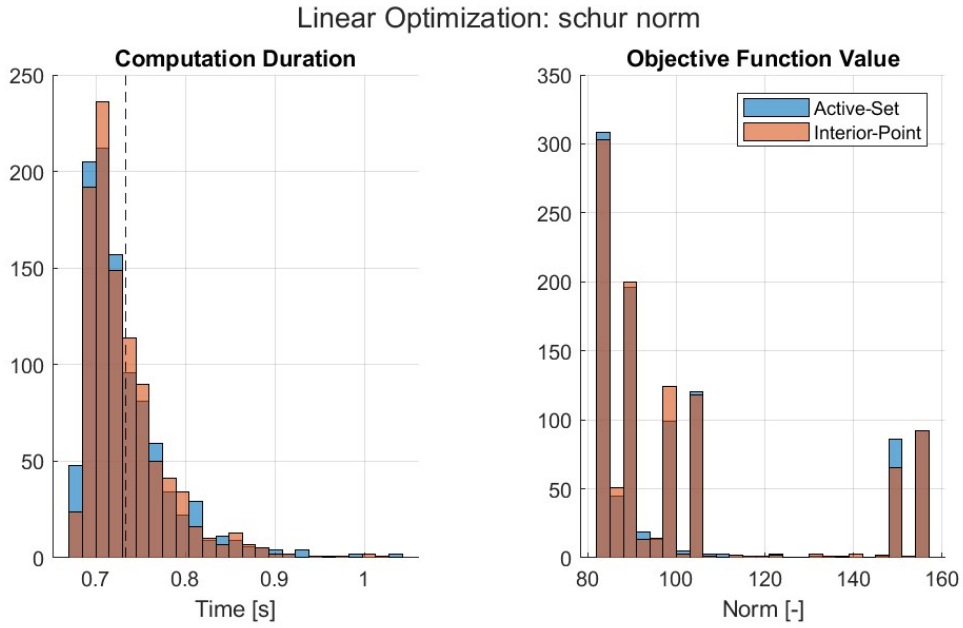

Figure 2.3: Constrained Linear Least Squares optimization algorithm comparison using Matlab's `lsqlin` function

The computational time of the active-set and interior-point algorithms were almost entirely identical ($\bar{t}_{as} = 0.7326s$ vs. $\bar{t}_{ip} = 0.7333$). Additionally, the average JCO norms are also very similar, with the interior-point slightly lower than the active-set ($\bar{B}(\mathbf{q})_{as} = 101.9218 vs. \bar{B}(\mathbf{q})_{as} = 100.9639$). Further analysis will use the active-set algorithm due to it being the algorithm used in [2] and [29].

Again, the significant kinematic configuration dependence of the JCO norm can be observed due to the multi-modal distribution of the objective function histogram. Choosing a different redundant configuration can cause the JCO norm to more than double for the

same end-effector pose and desired Cartesian stiffness matrix.

We can also compare the nonlinear solver examined in subsection 2.4.1 against the linear solver detailed above. This can be seen in Figure 2.4. Interestingly, the nonlinear solver is significantly faster than the corresponding linear solver. This is almost certainly due to the specific implementation in Matlab. While the `lslin` function was quicker to converge than the `fmincon` function, the process of linearizing $J(\mathbf{q})\mathbf{c}_{Jp}J(\mathbf{q})^{\mathsf{T}}$ was surprisingly computationally intensive. Additional work could be done to improve the efficiency of this operation, either through the algorithms presented in [13] or by implementing this in a different programming language without as much overhead as Matlab.

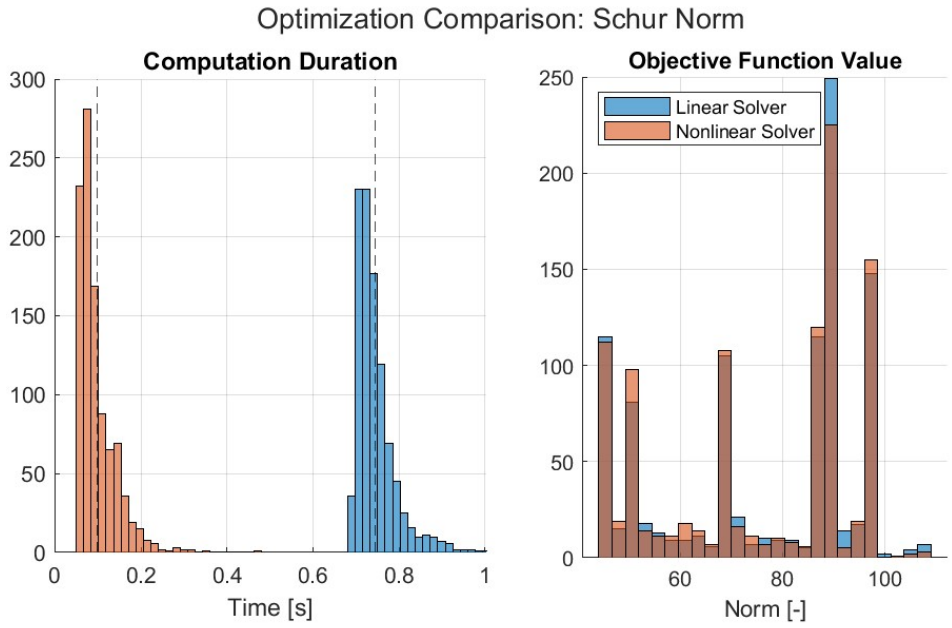

Figure 2.4: Nonlinear vs. Linear joint compliance algorithm comparison for a constant desired Cartesian stiffness matrix and end-effector pose

Given the increased speed of the nonlinear optimization, the Matlab `fmincon` using a SQP algorithm will be used as the basis for the following analysis.

2.5 Configuration Dependent Stiffness Optimization

For a redundant manipulator, there are an infinite number of joint configurations to achieve a desired end-effector pose. Figure 2.5 shows an example of a subset of the redundant configurations. Nullspace motions enable the manipulator to change its joint configuration without moving the end-effector. Existing inverse kinematic algorithms utilize the extra degrees of freedom by optimizing a secondary performance criterion [37]. This could involve avoiding kinematic singularities, minimizing the joint velocity norm, moving away from mechanical joint limits, or moving around environmental obstacles. The method of selecting the nullspace configuration through secondary performance criteria is called redundancy resolution.

In section 2.4, the considerable dependence of the robot configuration on the passive stiffness mapping performance was shown. As a result, this increase in performance can be achieved by augmenting the redundancy resolution method. This can be done either by adding an additional term to the redundancy cost function [2] or by extending the velocity Jacobian [31].

First, subsection 2.5.1 will examine how to derive the Jacobian nullspace base matrix, giving the linear subspace enabling the moving of joint positions without changing the end-effector position. This will be used in the gradient descent optimization routine, described in subsection 2.5.2, to reduce the passive stiffness mapping error.

2.5.1 Derivation of a Redundant Manipulator's Nullspace

To compute the manipulator's nullspace base matrix $N(\mathbf{q})$, the same formulation for a redundant manipulator will be used as was presented in section 2.1. For redundant manipulators, the degree of redundancy is defined as $r = n - m$. The most common situation for both manufacturing and space robotics has a 7 joint serial manipulator achieving a 6-

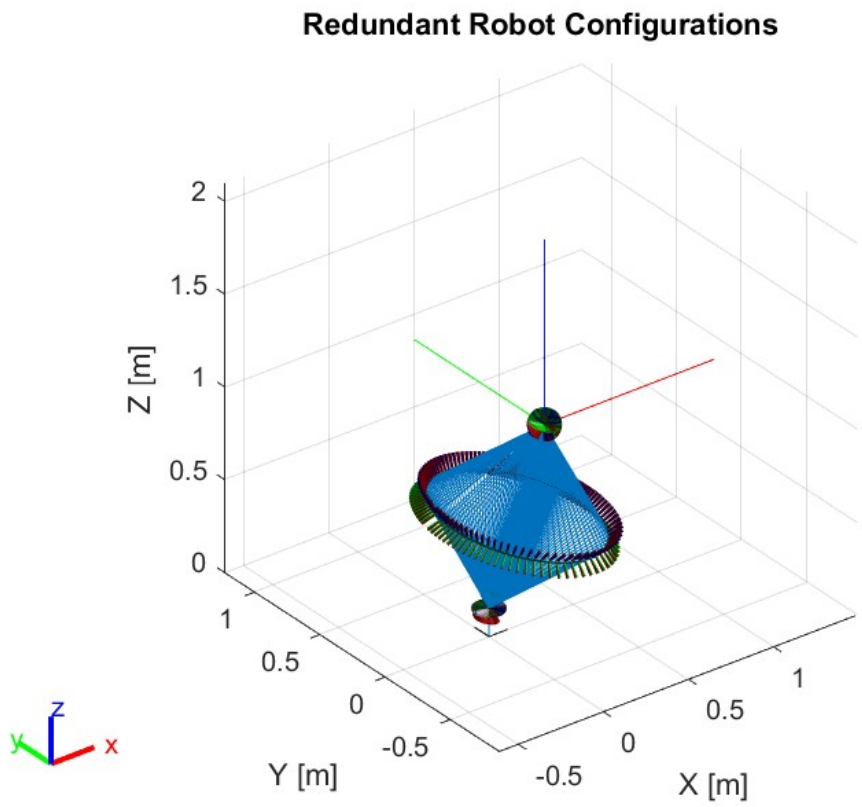

Figure 2.5: A subset of redundant joint configurations for a single end-effector Cartesian configuration

degree-of-freedom task, resulting in a 1-degree-of-freedom redundancy ($r = 7 - 6$). This extra degree of freedom enables the nullspace motions of the manipulator. The general case for computing the velocity Jacobian's nullspace base matrix is described in [8].

Since the robots examined in this thesis only have a single degree of redundancy ($r = 1$), the general form for calculating the nullspace base matrix can be simplified to a single row also according to [8]:

$$N(\mathbf{q} = \begin{bmatrix} n_1(\mathbf{q}) & \dots & n_r(\mathbf{q}) \end{bmatrix} \tag{2.18}$$

Where the elements of $n_i(\mathbf{q})$ can be computed as:

$$n_i(\mathbf{q}) = (-1)^{n+i} det(J_i(\mathbf{q})) \tag{2.19}$$

With $J_i(\mathbf{q}) \in \mathbb{R}^{m \times m}$ is the Jacobian matrix $J(\mathbf{q})$ with the i^{th} column omitted.

This method for extracting the Jacobian nullspace base matrix can now be used as part of an iterative optimization algorithm to minimize passive stiffness mapping errors.

2.5.2 Joint Compliance Redundancy Resolution

Utilizing the derivation of the Jacobian nullspace base matrix, a method can be developed to find the optimal manipulator configuration to minimize the passive stiffness mapping error. A method for using an iterative gradient descent algorithm for minimizing the passive stiffness mapping was proposed by [2] and [13]. This algorithm can be modified slightly by using the previously described nonlinear joint compliance optimization equation Equation 2.15 as the cost function.

$$B(\mathbf{q}, C_{Cd}) = \| C_{Cd} - J(\mathbf{q}) \mathbf{c}_{Jp} J(\mathbf{q})^{\mathsf{T}} \|_F^G \tag{2.20}$$

The locally valid update law to step through the Jacobian nullspace, as described in [13], becomes:

$$\mathbf{q}_{i+1} = \mathbf{q}_i - \alpha \nabla_{N_q} B(\mathbf{q}, C_{Cd}) \tag{2.21}$$

Where the gradient describes how much to move in the direction of the Jacobian nullspace base vector depending on the change in the joint compliance optimization norm. The gra-

dient is defined as:

$$\nabla_{N_q} B(\mathbf{q}, C_{\mathbf{Cd}}) = \lim_{h \to 0} \left(\sum_{i=1}^{r} \mathbf{n}_i(\mathbf{q}) \frac{B(\hat{\mathbf{q}}, C_{Cd}) - B(\mathbf{q}, C_{Cd})}{h} \right) \tag{2.22}$$

With $\hat{\mathbf{q}}$ defined as:

$$\hat{\mathbf{q}} = \mathbf{q} + h \cdot \mathbf{n}_i(\mathbf{q}) \tag{2.23}$$

In this formulation, $N(\mathbf{q})$ is the nullspace base matrix as defined in subsection 2.5.1. α and h are parameters that are used to tune the gradient descent algorithm. α determines the size of a step between each joint configuration. A large α will allow the algorithm to descend faster but will cause deviations in the end-effector position due to the nonlinear forward kinematics mapping.

Each algorithm iteration requires two separate joint compliance optimization subroutines, so depending on the number of iterations required to converge to a local minimum, the computation time could grow significantly. Restrictions to the computational time are required if such an algorithm were to be implemented in real-time as done by [13]. For offline trajectory planning, computational time is less of an issue, and additional performance can be achieved.

Additional algorithm exit criteria are required for practical implementation. The first exit criterion is a limit to the maximum number of iterations, which helps prevent any potential cyclical behavior of the algorithm. The second is a check against the validity of the joint configuration. Almost all physical robot actuators have some sort of mechanical joint limit, either through the inclusion of physical hard stops or due to the wrapping of harnessing, that will prevent rotation. The third exit criterion checks against potential self-collisions to prevent the manipulator from crashing into itself. This could be extended to include environment collision detection but would require a detailed understanding of the

robot system's environment. The final exit criteria is a check that the stiffness mapping gradient from Equation 2.22 is larger than a given tolerance. This tolerance can be tuned depending on a trade-off between computation time and increased performance.

The passive stiffness mapping is highly nonlinear, with a significant amount of local minima. An example configuration dependent stiffness optimization can be seen in Figure 2.6. For an initial inverse kinematics solution, the joint configuration was moved through the nullspace motions until arriving back at the initial IK solution. For each configuration, the joint compliance optimization norm is computed per Equation 2.20. The red regions of the figure are the domains that exceed joint limits or result in self-collisions. The blue star indicates the global minimum.

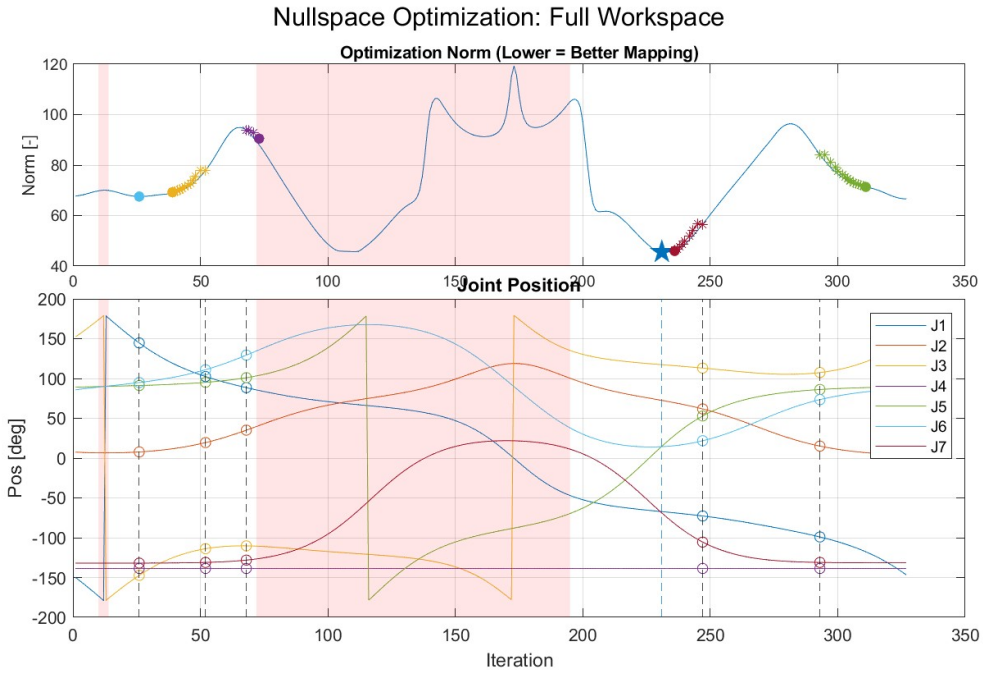

Figure 2.6: Full workspace passive stiffness mapping optimization with five gradient descent optimizations.

Five different initial conditions were used for the iterative gradient descent algorithm with results plotted on Figure 2.6. The initial conditions are the vertical black dashed lines

on the position subplot. Each iteration of the optimization is plotted with a star, while the final iteration is plotted with a filled-in circle. Of the five initial conditions, only one was able to find the global minimum due to the presence of nine local minima. As a result, even with multiple cold starts, the gradient descent algorithm is not guaranteed to find the global minimum. However, the benefit of the iterative gradient descent algorithm is observed and is able to increase the performance of the passive stiffness mapping by $20\% - 50\%$ depending on the initial configuration. This can potentially be improved by using different algorithms, such as the conjugate gradient descent method.

2.6 Sequential Passive/Active Stiffness Optimization

Even through the exportation of the redundant configurations of a serial manipulator, the diagonal nature of the joint stiffness matrix makes it difficult for a variable-stiffness robot to achieve an arbitrary Cartesian stiffness matrix. One potential method for increasing the stiffness mapping performance proposed by [29], and expanded in [13], uses an active impedance controller in addition to passive stiffness control. This method enables such a robot to maintain the beneficial shock absorbing, energy saving, and stiffness variation at constant position properties of the elastic stiffness element while being able to maintain an exact Cartesian stiffness. However, the manipulator now requires a force-torque sensor to accurately measure the external disturbances to implement the active controller.

A brief introduction to using active Cartesian stiffness control in flexible robots is discussed in subsection 2.6.1, and the implementation into a sequential stiffness mapping algorithm is discussed in subsection 2.6.2.

2.6.1 Active Stiffness Mapping

The desire for a robot manipulator to not only track a desired reference trajectory but also control the behavior of loads imparted to its environment is one of the fundamental challenges when controlling serial manipulators. Methods of active force control are surveyed in [25], and the application of active impedance control for flexible joint robots are examined in detail in [8].

The impedance controller can either be formulated in joint space or Cartesian space depending on the requirements of the task [25]. A joint space formulation is commonly used for tasks less sensitive to the exact compliance properties if it might approach kinematic singularities, due to its ability to limit joint velocities in those regimes. Some examples include visual servoing, grappling free-flying objects, or dual arm control [20]. For tasks with sensitive compliance dynamics, a Cartesian space formulation is often used as long as the tasks can be planned to be performed in areas of the workspace away from the undesirable kinematic singularity effects.

A joint space formulation of an active impedance algorithm for variable stiffness robots was proposed in [2]. A Cartesian space formulation for variable stiffness robots was first examined in [29], and later [13]. Given the desire for the ability to specify desired compliance dynamics, the Cartesian space formulation will be examined, and special considerations will be made during task/trajectory planning to ensure singularity avoidance.

The active Cartesian impedance control law, explored in [29], is as follows:

$$F_{imp} = -K_{Ca}(\mathbf{x} - \mathbf{x}_d) - D_C\dot{\mathbf{x}} \tag{2.24}$$

Where K_C is the Cartesian stiffness matrix of the impedance controller and D_{Ca} is the Cartesian damping matrix. The selection of D_C is heavily examined in [13], and will not

be examined in detail here. The question becomes how to choose D_{Ca} to obtain the optimal Cartesian stiffness mapping. The method of reducing Equation 2.15 to only optimize the active Compliance matrix is taken from [29], with a few minor modifications to be consistent with the formulations and assumptions in this text.

$$\begin{aligned} &\underset{C_{Ca}}{min} \|C_{Cd} - C_C(C_{Ca})\| \\ &s.t. C_{Ca} > \mathbf{0} \end{aligned} \tag{2.25}$$

Where the active Compliance matrix C_{Ca} must be positive definite to maintain passivity properties to ensure the stability of Equation 2.24. This can be solved using a matrix nearness problem through an eigenvalue transformation of both the desired and active compliance matrices. By replacing non-positive eigenvalues of the transformed compliance matrix with a small, positive compliance value, the active Compliance matrix can be assured to be positive-definite, with some induced error. These eigenvalues are then transformed back into the rotated, Cartesian end-effector frame.

2.6.2 Sequential Stiffness Mapping

The addition of active Stiffness control is able to extend the achievable Cartesian stiffness range. However, the motivation is to still use the passive stiffness method as much as possible to maintain the unique properties of the passive stiffness element. As a result, a sequential stiffness mapping method was developed by [29] to first use the passive joint stiffness adjustments as much as possible, and then add an additional active method to help reduce remaining errors.

To evaluate the performance of the sequential algorithm, the computation time and

sensitivity to robot configuration were evaluated. This can be seen in Figure 2.7.

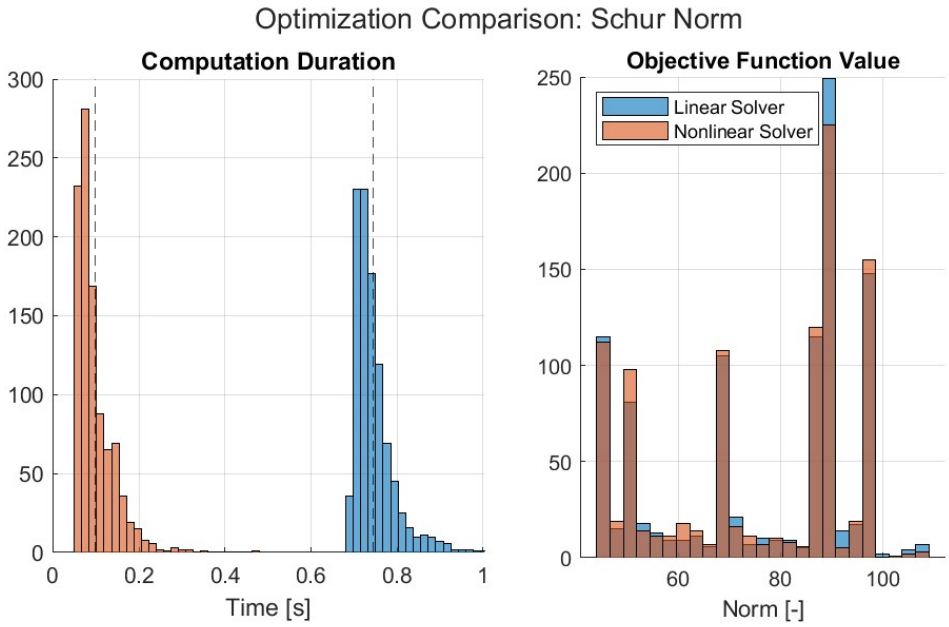

Figure 2.7: Sequential Optimization Performance: Algorithm first performs a passive joint stiffness optimization using a nonlinear solver, and then performs an active Cartesian stiffness optimization using a matrix nearness approach.

Using sequential stiffness mapping, the residual Cartesian stiffness errors are able to be reduced by two orders of magnitude when compared to the strictly passive methods. This makes sense given the active algorithm no longer has the restriction of using a diagonal joint stiffness matrix. Again, the average duration of the sequential algorithm is only slightly longer than the strictly passive method given the relative simplicity of performing the matrix nearness optimization.

2.7 Discussion

Three different methods of joint stiffness optimization were examined; a passive method, a configuration-dependent passive method, and finally a sequential active/passive method. These methods all have their own benefits and trade-offs and can be used for different

applications of joint stiffness optimization which will be examined later in chapter 4 and chapter 5. While the work presented in this thesis only examines the offline task and trajectory planning considerations, there are additional considerations to be taken into account if online optimization is needed.

Chapter 3: Task Definition

Given the research questions proposed in section 1.3, a well-defined task is needed to understand the effects on the passive stiffness realization performance. The hope is that while the following analysis is less applicable to different applications, the proposed methods and analysis techniques could be used to design a variable-stiffness robot for a diverse population of potential tasks.

To develop these analysis methods and understand their sensitivity, the robot kinematics, VSA parameters, and desired Cartesian compliance will be taken from previous as-tested results and published literature. This will ensure that the results of this work can directly be compared to existing ISAM and ADR missions.

3.1 Ranger Dexterous Manipulator

The Ranger dexterous manipulator is a space-qualified redundant serial manipulator designed and built by the University of Maryland Space Systems Laboratory for the Ranger satellite servicing system [32]. First considered for a Space Shuttle flight experiment, and later for Hubble Space Telescope servicing, Ranger is designed to be operated on the ground, in space, and in neutral buoyancy. Consisting of 8 degrees of freedom, the manipulator was designed to provide similar dexterity and force capability as an astronaut in EVA. A force-torque sensor mounted at the end-effector to enable the implementation of an active impedance control algorithm. This active impedance control was evaluated in [33].

Figure 3.1: Ranger Dexterous Manipulator

The robot kinematics can be described by the Denavit-Hartenberg (D-H) parameters in Table 3.1 and are taken from [7]. The Ranger arm is unique in that it contains a 4-degree-of-freedom spherical wrist. This results in the first four joints mainly for positioning the end-effector in Cartesian space and the remaining joints are used to control the end-effector orientation.

Table 3.1: Ranger D-H Parameters (8-DoF)

Link	a_{i-1} **(cm)**	α_{i-1} **(rad)**	d_i **(cm)**	θ_i **(rad)**
1	0	0	15.24	θ_1
2	0	$\pi/2$	0	θ_2
3	0	$-\pi/2$	53.89	θ_3
4	0	$\pi/2$	0	θ_4
5	15.24	$-\pi/2$	51.17	θ_5
6	0	$\pi/4$	0	θ_6
7	0	$\pi/2$	0	θ_7
8	0	$-\pi/2$	0	θ_8

This thesis will use the kinematics of the Ranger dexterous manipulator for the design reference missions given its direct task applicability, and significant existing published literature. Each Ranger joint will be replaced with a VSA, doubling the number of degrees-of-

freedom, and providing the desired passive stiffness behavior. Two different configurations will be considered for future analysis. The first is to lock the 6th joint position, effectively creating a 7-DoF manipulator. Given most existing space manipulators only have 7-DoFs [20], this simplification will ensure the results are more useful for existing comparisons. Additionally, the full 8-DoF configuration will also be examined to understand the effects of adding additional degrees of redundancy.

3.2 VSA Mechanical Stiffness Limits

While the VSA level controller and internal dynamics are not needed for this thesis, the joint stiffness upper and lower limits are required to evaluate passive stiffness realization. Three different VSA joint stiffness limits will be examined; AwAS-II, FSJ, and FSJ-Extended. These three actuators were chosen due to having physical test data and encompassing the most common configurations of VSAs. A description of the AwAS-II and FSJ can be found previously in subsection 1.2.1. The joint stiffness limits used for the three test configurations can be found in Table 3.2.

Table 3.2: VSA Joint Stiffness Limits

VSA Name	k_j^{min}	k_j^{max}
AwAS-II	0.5	2000
FSJ	50	830
FSJ-Extended	50	15000

Using the AwAS-II joint stiffness limits, one can examine how lowering the joint stiffness affects the realization performance. It is interesting to note that on Earth, a joint stiffness of $0.5 Nm/rad$ would not be feasible due to the gravitational and inertial forces within the manipulator. These additional forces could deflect the passive stiffness element all the way to a mechanical limit, effectively shunting any compliant behavior in the actuator. However, since the proposed ISAM task would be performed in zero gravity, the

lower bound of the joint stiffness can be reduced without the worry of hitting a mechanical deflection limit.

Conversely, the FSJ-Extended joint is a theoretical modification version of the FSJ joint, increasing the upper stiffness bound to that of a typical rigid robot joint [13]. By enabling the joint stiffness to be increased to $15000 Nm/rad$, the effects of the upper stiffness bound can be tested. Increasing the upper joint stiffness limit would not be physically practical. This is because most VSAs function by adding a compliant element in series with a traditional robot joint. Increasing the joint stiffness above that of a traditional robot joint would require an entirely different joint mechanical design.

3.3 Trajectory Task and Stiffness Requirements

Even for ISAM and ADR applications, the end-effector's trajectory and stiffness requirements can vary significantly depending on the mass and inertia of the servicing satellite as well as the resident space object (RSO). The lighter the two objects, the lower Cartesian stiffness is required to ensure a successful grapple. To help simplify the analysis in this thesis, the trajectory and stiffness requirements will be taken from [19]. In this paper, the authors developed and validated a framework for determining the contact dynamics for a servicer satellite to grapple a RSO using a 7-DoF manipulator. A simulation framework for predicting the free-floating contact dynamics was developed and validated with ground tests using a rigidly mounted manipulator grappling a servicer mounted to a sled floating on a granite table. The paper reports the compliance gains used, as well as the separation rates between the end-effector and the sled to determine if a capture would be successful.

The initial conditions used in the paper can be turned into a series of system requirements that can be found in Table 3.3. These system requirements can then be flowed down to a series of task and stiffness requirements for future manipulator workspace analysis.

To ensure a successful grapple, the separation rates between the servicer and client after first-contact need to be properly managed. If the client drifts too far away from the servicer before the grapple end-effector's fingers can close, the client will fail to be captured.

Table 3.3: System Requirements for RSO Grapple from [19]

Requirement	Name	Description
R-1	Servicer Mass	The servicer satellite shall have a mass of 2100kg
R-2	RSO Mass	The client satellite shall be assumed to have a mass of 3800kg
R-3	Grapple Velocity	The grapple end-effector shall move towards the RSO at a velocity of 1cm/s
R-4	Grapple Duration	The grapple end-effector shall be able to close within 2 seconds of initiation
R-5	Separation Distance	The client shall remain within 0.75cm of the grapple end-effector during the grapple duration
R-6	Tracking Knowledge Error	The manipulator shall be able to follow a reference trajectory within *TBD* 1σ bounds
R-7	Client State Knowledge Error	The servicer shall maintain 6-DoF state knowledge of the client within *TBD* 1σ bounds

The authors of [19] implemented a joint-level compliance control algorithm to evaluate the Cartesian stiffness parameters to ensure a successful grapple. Initial simulations predicted Cartesian stiffness gains of $[k_x \;\; k_y \;\; k_z] = [41.7 \;\; 39.5 \;\; 181.6] N/m$ would enable successful grapple (where $+z$ is the contact direction). During testing, it was found that these gains caused the sled to bounce back and forth between the grapple end-effector's fingers, which could reduce the chance of grapple success. As a result, the lateral Cartesian stiffness gain was increased slightly to $[k_x \;\; k_y \;\; k_z] = [114.5 \;\; 127.8 \;\; 187] N/m$ to minimize this initial instability. These Cartesian stiffness gains will be used for future passive stiffness realization analysis.

While [19] published Cartesian stiffness gains which enable successful grapple of an RSO, the authors did not publish the torsional stiffness gains used. This is because, for planar testing with a sled and granite table to simulate zero gravity, the reduced dimensional

system does not require all six stiffness gains. As a result, four different sets of torsional stiffness gains were examined for their effect on passive stiffness realization. These different configurations of the desired Cartesian stiffness matrix are listed in Table 3.4. The range of torsional stiffness gains was chosen to evaluate how changing these gains affects the passive stiffness realization performance.

Table 3.4: Desired Cartesian Stiffness (K_{cd}) Cases

#	k_{dx}	k_{dy}	k_{dz}	k_{rx}	k_{ry}	k_{rz}
–	N/m	N/m	N/m	Nm/rad	Nm/rad	Nm/rad
1	120	120	190	25	25	40
2	120	120	190	100	100	160
3	120	120	190	800	500	500
4	120	120	190	1000	1000	250

3.4 Trajectory Requirements

While the system requirements are important for defining the interface between the servicer and the RSO, they do not provide manipulator performance requirements or pass/fail design criteria. Thus these system requirements need to be distilled to the manipulator level to help aid the design of the manipulator and analysis of the workspace. These manipulator-level trajectory requirements can be divided into two sub-categories; task and stiffness realization. These trajectory requirements can be found in Table 3.5, with R-101 through R-104 being the task requirements and R-201 through R-202 being the stiffness realization requirements.

These manipulator-level requirements can be used to further analyze the regions of the workspace where passive stiffness control can be used effectively. The task requirements give restrictions on the shape of the candidate trajectories, while the stiffness realization requirements determine whether passive stiffness control is effective in managing the contact dynamics.

Table 3.5: Manipulator Trajectory Requirements

Rqt	Name	Description	Source
R-101	Direction	A grapple shall be performed in either the horizontal, vertical, or radial direction with respect to the robot origin frame	R-5
R-102	Velocity	A grapple shall be performed at a velocity of 1cm/s	R-3
R-103	Duration	A grapple shall last a minimum of 20 seconds	R-4, R-5
R-104	Misalignment	A grapple shall be able to accommodate a lateral misalignment of TBD cm	R-6, R-7
R-201	Desired Stiffness	The desired Cartesian stiffness shall be selected according to Table 3.4	R-1, R-2, R-5
R-202	Realization Error	The maximum realization error shall be ε	R-1, R-2, R-5

Chapter 4: Kinematic Workspace Analysis

The ability of a robot arm to manipulate objects within its environment requires the ability to specify both the position and the orientation of its end-effector. It is relatively simple to understand and visualize the spatial dependency on where a robot arm can interact with objects, however, certain regions of the workspace can only be reached from specific directions. Describing this directionality is of high importance, especially when considering trajectory or grasp planning within the workspace.

This chapter will look to examine how to describe the dexterous workspace as an attempt to find an existing measure or analysis that can be used to inform the creation of feasible stiffness mapping regions.

4.1 Dexterous Workspace Index

A robot workspace is defined as the set of task-space poses ($\mathbf{x} \in \mathbb{R}^n$) that are achievable for a given manipulator's kinematic geometry. The robot workspace can be further divided into the reachable and dexterous workspace. For a reference point on the robot end-effector, the reachable workspace is the set of all Cartesian points that can be reached by the robot. The reachable workspace can be calculated in different ways, but the most common is the monte carlo approach introduced in [18], involving random sampling of joint-space configurations which are then propagated to task space using forward kinematics. For a standard 6-DoF ($n = 6$) Cartesian workspace, the reachable workspace provides

a pass/fail criteria for if a given 3-DoF position $P = (x, y, z)$ can be reached without regard to orientation. While useful to provide a general envelope of the reach of a robot arm, the reachable workspace provides no information on the directional structure or potential trajectories that could pass through point P.

Alternatively, the dexterous workspace is a subset of the reachable workspace where a point p can be reached with some arbitrary number of orientations. To analyze the dexterity, a modified version of the capability map approach proposed in [43] was used. A hemisphere with a radius slightly larger than the reach of the arm was created, and then discretized into a series of points given in polar coordinates $p = (\phi, \theta, r)$. For each discretized element, an inscribed sphere was then generated with N points equally distributed across the surface [34]. For each point obtained on the inscribed sphere, a desired reference frame is generated with the z-axis (blue) pointing towards its center and the x-axis (red) and y-axis (green) tangential to the sphere. Each frame is then rotated about its z-axis to create M rotated reference frames per point $n \in N$. The process to generate the set of possible end-effector frames can be seen in Figure 4.1.

For each end-effector frame generated, an inverse kinematic solution is then calculated to determine if the desired end-effector frame is a valid task-space configuration of the robot arm. If a valid inverse kinematic solution exists that satisfies the joint limits without any self-collisions or singularities, the end-effector frame is considered to be a feasible solution. If any of the rotated reference frames M at a point n contains a feasible inverse kinematic solution, that point n is considered a feasible orientation. The number of feasible orientations R is the total number of points $n \in N$ which contain at least one feasible reference frame m.

$$D = R/N * 100 \tag{4.1}$$

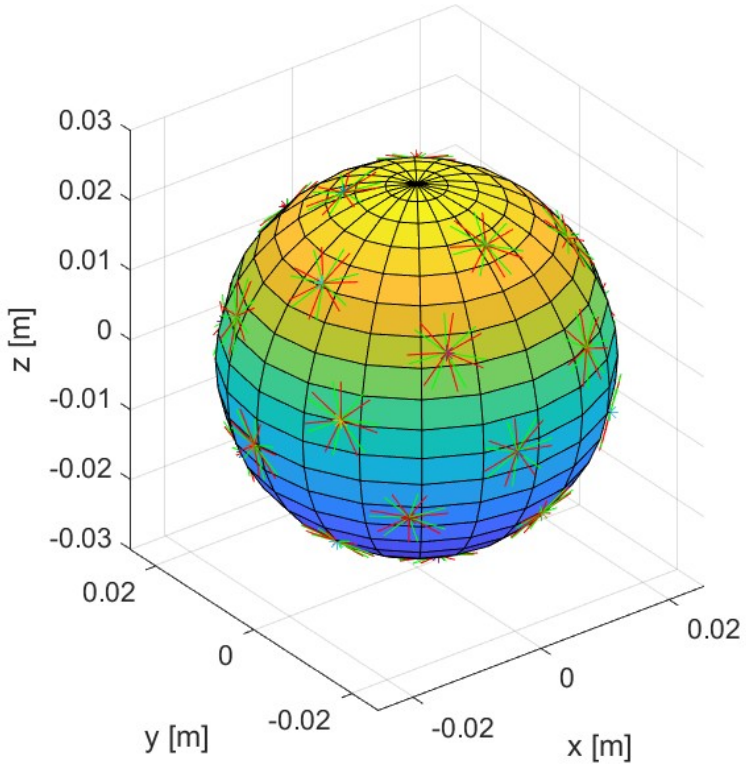

Figure 4.1: Desired End-Effector Frames on an Inscribed Sphere

For each discretized element, the Dexterity Index D is computed according to Equation 4.1, where N is the total number of points distributed on the surface of the inscribed sphere and R is the subset of N which have a feasible solution. The Dexterity Index D can then be examined across the entire reachable workspace to understand the regions of the workspace which enable the robot arm to move in most directions with ease.

4.2 RANGER Dexterous Workspace Analysis

The dexterous workspace was analyzed for the RANGER robot arm described in section 3.1 using the methodology laid out in section 4.1. However, a slight modification was made in the method of generating desired reference frames due to the nature of the appli-

cations listed in chapter 3. The required trajectories for both grappling client spacecraft and active debris removal employ the manipulator moving in the end-effector's positive z-axis away from the base of the robot arm. This results in the arm always moving away or tangential to the manipulator base. Thus, instead of generating N frames equally distributed across the entire surface of each inscribed sphere, only reference frames where the z-axis points away from the origin were considered. An example of the desired end-effector frames generated for each discretized element of the reachable workspace is seen in Figure 4.2. This modification is consistent with the dexterity analysis performed in [9] for the Front-End Robotics Enabling Near-Term Demonstration (FREND) space manipulator.

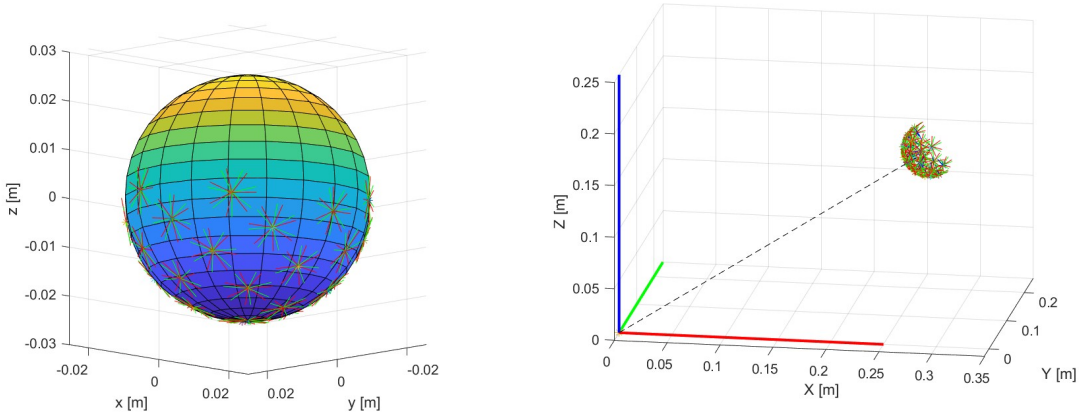

(a) Axis align with inscribed hemisphere

(b) Inscribed hemisphere with respect to robot base

Figure 4.2: Desired End-Effector Frames on an Inscribed Hemisphere

As mentioned in section 3.1, the RANGER robot arm has two unique features that aid in the analysis of its dexterous workspace. The first is that the hardware joint limits for the first actuator (Shoulder Yaw) are greater than 360 degrees. This results in both the reachable and dexterous workspace containing rotational symmetry about the $\hat{\mathbf{z}}_0$ axis. The second is that the last three joints (5, 6, and 7) all have intersecting rotation axis, resulting in a spherical wrist. This is highly beneficial because it enables the decoupling of a desired Cartesian configuration into a position and orientation sub-task. The parameters used for

the Ranger robot arm dexterity analysis can be found in Table 4.1.

Table 4.1: Ranger Dexterity Analysis Parameters

Parameter	Symbol	Units	Min	Max	Steps
Azimuth	ϕ	rad	0	π	17
Elevation	θ	rad	0	$\pi/2$	30
Radius	r	m	0.25	1.5	25
Z-axis Rotation	M	#	-	-	8
Points on Hemisphere	N	#	-	-	30

The dexterous workspace index analysis results can be found in Figure 4.3. A point will be considered dexterous if the Dexterous Index is above 75%, which is consistent with the methodology in [9]. Most of the workspace has a Dexterity Index of 100% thanks to the spherical wrist and careful considerations when determining joint limits. The two regions where the Dexterity Index drops are at the boundary of the workspace. This is due to the rotation axis of joint 2 (Shoulder Pitch) being $15.24cm$ above the robot origin, preventing it from reaching all the way to the bottom of the workspace boundary. The other decrease in the Dexterity Index is nearby the robot's origin due to self-collisions. Again, this region is centered $15.24cm$ above the robot origin due to the link 1 offset. The dexterous workspace is more uniform for the Ranger arm than for the FREND arm found in [9]. This is due not only due to the advantageous geometry of the Ranger arm but also due to [9] including a singularity avoidance and non-cyclical motion weighting term in the pseudo-inverse used for Cartesian to joint space mapping. Due to using redundant joint nullspace for increasing the performance of joint-to-Cartesian stiffness mapping, a different method of singularity avoidance and detection is needed.

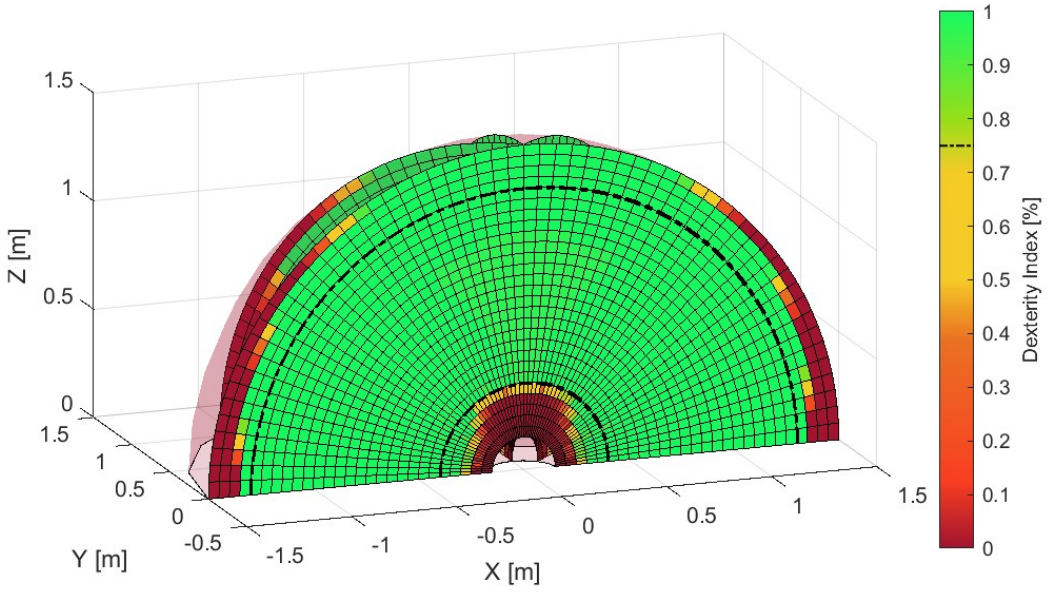

Figure 4.3: Ranger Dexterous Workspace Index

Chapter 5: Passive Stiffness Workspace Analysis

Now that passive stiffness realization methods have been implemented in chapter 2 and the task has been well defined in chapter 3, one can finally attempt to answer the proposed research questions.

1. For a single, well-defined task, are there regions of the workspace where a prescribed level of passive stiffness realization can be achieved?

2. For a mobile robot, can we plan trajectories within a region of the workspace to improve realization performance?

First, the impact of trajectory direction will be examined through the creation of Feasible Stiffability Maps in section 5.1. Then, the idea of Successful Task/Stiffness Trajectories and Successful Task/Stiffness Regions (STSR) will be introduced in section 5.2. The shape and volume of these STSRs will be used to answer the first research question. Next, the sensitivity of STSRs to changes in the Mechanical Joint Stiffness Limits and degrees of redundancy will be examined in section 5.3 and section 5.4.

5.1 Feasible Stiffability Maps

Feasible Stiffability Maps (FSM) are a three-dimensional extension of the stiffability maps described in subsection 1.2.3. They provide a way of examining the workspace and directional dependency of the passive stiffness realization. Stiffability maps were initially

proposed in [13] to provide a way to visualize the Cartesian stiffness principle axes for a two-dimensional planar manipulator. This idea will be extended into the third-dimension to provide a way of evaluating the passive stiffness realization for an arbitrary manipulator.

These three-dimensional stiffability maps are generated by performing the passive stiffness realization optimization across the entire dexterous workspace. Each point in the dexterous workspace can be reached from a series of different end-effector orientations, three different end-effector trajectory configurations were considered:

1. Horizontal: $+\hat{\mathbf{z}}_{ee}$ is moved in the positive $+\hat{\mathbf{x}}_0$ direction
2. Vertical: $+\hat{\mathbf{z}}_{ee}$ is moved in the positive $+\hat{\mathbf{z}}_0$ direction
3. Radial: $+\hat{\mathbf{z}}_{ee}$ is moved in a straight line away from the origin of the manipulator

These three configurations encompass almost all feasible directions of the end-effector thanks to the symmetry of the manipulator and the absence of joint limits on the first joint. This axial symmetry about the $+\hat{\mathbf{z}}_0$ axis results in trajectories in the $+\hat{\mathbf{y}}_0$, or any direction parallel to the ground plane, to be represented as trajectories in the $+\hat{\mathbf{x}}_0$ direction. Trajectories performed in the $-\hat{\mathbf{z}}_0$ direction are not examined, due to not being representative of a grapple for ISAM and ADR tasks.

For each of the three end-effector trajectory directions, joint stiffness optimization is then performed across a discretized dexterous workspace. At each position and orientation, the Constrained Passive Joint Stiffness (CPJS) optimization was performed according to the methods described in section 2.4. For the CPJS, a test matrix was developed from the joint stiffness limits listed in Table 3.2 and desired Cartesian stiffness matrices from Table 3.4. The full test matrix can be found in Appendix A. For each CPJS optimization, 10 cold starts are used to attempt to find the global minima of the CPJS cost function. The cost function is then normalized according to Equation 5.1, and the results are plotted for each

element. Example results for the 14th test index showing the effect of different trajectory directions can be found in Figure 5.1, Figure 5.2, and Figure 5.3.

$$B = \frac{\|K_{Cd} - K_{Cp}\|_F^G}{\|K_{Cd}\|_F^G} \tag{5.1}$$

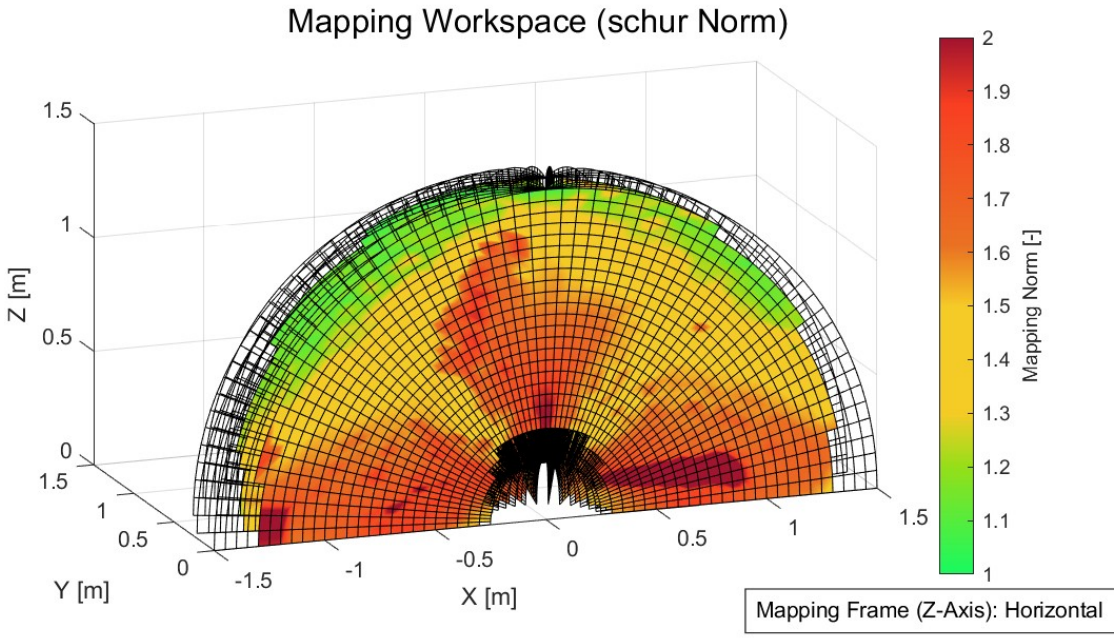

Figure 5.1: Horizontal ($+\hat{\mathbf{x}}_0$): $k_{cd} = [120\ \ 120\ \ 190\ \ 1000\ \ 1000\ \ 250]$, $k_{jl} = [50\ \ 830]$

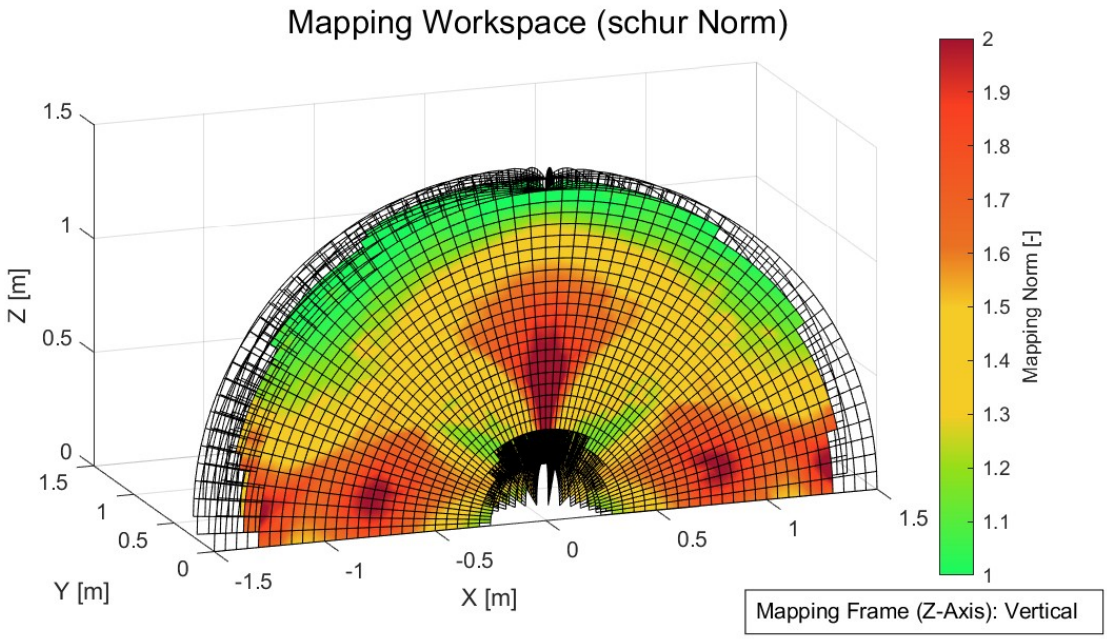

Figure 5.2: Vertical ($+\hat{\mathbf{z}}_0$): $k_{cd} = [120 \;\; 120 \;\; 190 \;\; 1000 \;\; 1000 \;\; 250]$, $k_{jl} = [50 \;\; 830]$

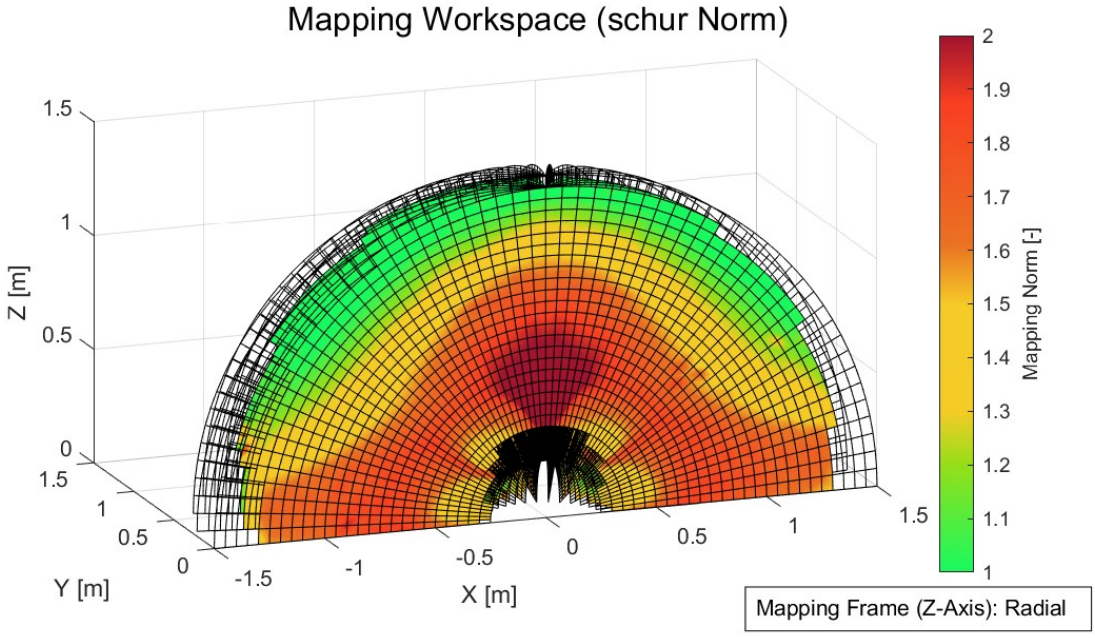

Figure 5.3: Radial: $k_{cd} = [120 \;\; 120 \;\; 190 \;\; 1000 \;\; 1000 \;\; 250]$, $k_{jl} = [50 \;\; 830]$

It is important to note that varying the joint stiffness limits and desired Cartesian stiff-

ness matrix will result in widely different Feasible Stiffability Maps. However, there are certain conclusions that can be made which are applicable generally. For all three trajectory directions, the singularity directly above the origin of the manipulator results in significantly degraded passive stiffness realization performance. Additional singularities (such as the $+\hat{\mathbf{y}}_0$ and $-\hat{\mathbf{y}}_0$ in Figure 5.2) also result in degraded realization performance. This is because, at these singularities the redundant degree of freedom disappears, resulting in only a single solution to the CPJS optimization. Other singularities are not as prominent as the $+\hat{\mathbf{z}}_0$ singularity due to having a kinematic configuration that allows for a larger range of possible Cartesian stiffness matrices.

Another conclusion that can be made strictly for this test configuration is that the exterior shell of the dexterous workspace, or where the manipulator is almost fully extended, is the region with the best passive stiffness realization. This is only valid for this test configuration due to the high lateral torsional stiffness gains. For test configurations with lower torsional stiffness gains, the interior of the dexterous workspace might contain the best stiffness realization performance. As a result, these Feasible Stiffability Maps need to be generated for and kinematic and joint stiffness parameters as well as the desired Cartesian stiffness matrix.

5.2 Task/Stiffness Trajectories

While certain conclusions, such as which areas of the workspace contain the best passive stiffness realization, can be made from Feasible Stiffability Maps, they do not provide any information on whether a valid trajectory can be performed. To help inform the understanding of regions of the workspace where valid trajectories can be executed, this thesis will introduce the idea of Task/Stiffness trajectories.

Given the manipulator requirements defined in Table 3.5, a series of candidate trajecto-

ries can be generated and evaluated against the task and stiffness realization requirements. Successful Task/Stiffness Trajectories (STST) are defined as the trajectories that are able to meet both the task and stiffness requirements. The region of the workspace for which a STST exists is defined as the Successful Task/Stiffness Region (STSR). A block diagram showing the relationship between these different sub-categories can be found in Figure 5.4.

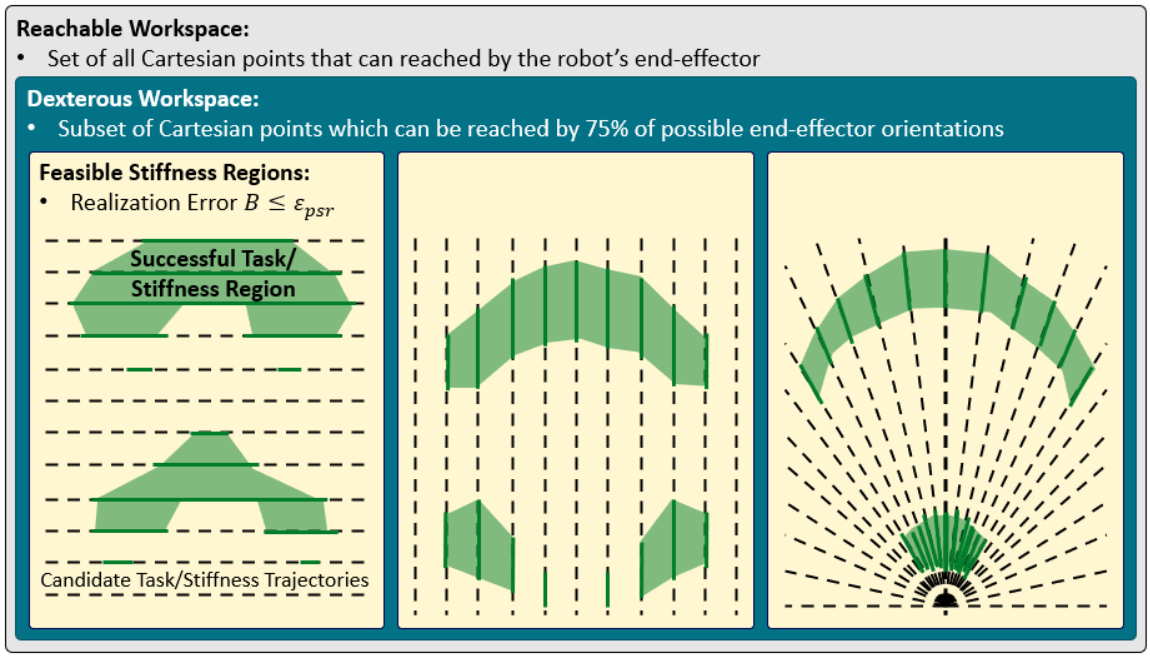

Figure 5.4: Block diagram showing the generation of STST and STSR for a given robot manipulator

To find the STST and STSR first, a series of Candidate-Task/Stiffness Trajectories are generated. For linear trajectories, such as grappling an RSO, a series of candidate trajectories are generated for each $+\hat{\mathbf{z}}_{ee}$ grapple direction. This is done by creating a mesh grid normal to the $+\hat{\mathbf{z}}_{ee}$ vector with a constant lateral spacing. For each position in the mesh grid, a trajectory is generated parallel to the $+\hat{\mathbf{z}}_{ee}$ vector. Any points on the trajectories not within the dexterous workspace are discarded, and the remainder become the Candidate-Task/Stiffness Trajectories. By decreasing the spacing between candidate trajectories, more details of the STSR can be realized at the expense of additional computational time. Addi-

tionally, the spacing between points on a given trajectory can also be increased or decreased also at the cost of additional computational time. It was found that is more critical to have a finer spacing between points on a given trajectory to ensure any interior geometry is properly captured.

Once the Candidate-Task/Stiffness Trajectories are generated, the CPJS optimization is performed for every point on each trajectory to evaluate the passive realization performance. This can be performed in two methods, depending on whether a restriction on ensuring each trajectory has a smooth joint ($\mathbf{q}$) and stiffness adjuster (σ) position. For the general case where a smooth trajectory is not required, the same CPJS optimization used to generate Feasible Stiffability Maps can be used. To determine the STST, first any points on a trajectory in which the CPJS cost function exceeds some threshold ε_{psr} are discarded. Next, any segments which are not valid for longer than some distance δ_{trj} are also discarded. What is left are the STST that meets both the task and stiffness manipulator requirements.

Once the STST are determined for a given realization threshold ε_{psr} and trajectory length δ_{trj}, a series of alpha shapes are generated. Alpha shapes are used in computational geometry to create a bounding area or volume that envelops a set of 2-D or 3-D points. The STSR is considered the series of alpha shapes required to fully enclose all STST. Example STSR are shown in Figure 5.5.

The STSR are shown for the three different end-effector trajectory configurations, horizontal (orange), vertical (green), and radial (blue). The wireframes are the regions of the workspace that meet the stiffness realization requirements ($B_{CPJS} \leq \varepsilon_{psr}$. The shaded regions represent the STSR which meets both the task and stiffness requirements.

Figure 5.5 shows the variation in the shape and volume of the STSR for a constant desired Cartesian stiffness matrix and realization threshold. The effect of selecting proper joint limits can be seen clearly due to the STSR in Figure 5.5a almost completely encom-

passing the dexterous workspace. The STSR in Figure 5.5b and Figure 5.5c are significantly smaller. Additionally, the grapple trajectory direction doesn't change the STSR volume significantly, but it does change the shape. The corresponding STSR volumes and number of STST for each trajectory direction can be found in Table 5.1.

Table 5.1: STSR Performance Parameters (Test Condition 14)

VSA	**Direction**	**STST**	**CTST**	**Percent Successful**	**STSR**
	-	#	#	%	m^3
AwAS-II	Horizontal	5877	10201	58%	5.12
	Vertical	5605	10201	55%	5.09
	Radial	5100	5100	100%	5.17
FSJ	Horizontal	751	10201	7%	0.14
	Vertical	309	10201	3%	0.05
	Radial	324	5100	6%	0.05
FSJ-Ext	Horizontal	829	10201	8%	0.13
	Vertical	332	10201	3%	0.08
	Radial	308	5100	6%	0.05

Additionally, the effect of changing the desired torsional stiffness gains can also be examined in Figure 5.6. To help aid in the visualization, the STSR graphs are clipped on the XZ plane to help view the internal geometry. Notice that the STSR volume increases as the torsional gains are also increased. Additionally, the semi-major axis of each STSR is largest in the direction of the grapple direction. For example, the horizontal (orange) STSR volumes are more squat than the vertical (green) STSR volumes. And the radial (blue) STSR volumes are more spherical in shape than the other trajectory directions (excluding the peak in the $+\hat{\mathbf{z}}_0$ direction). Additional results can be found in Appendix A.

The previous results all used a method for determining the passive realization performance without requiring the joint $(\mathbf{q})$ and stiffness adjuster (σ) positions to be smooth across the entire trajectory. For a redundant manipulator, the CPJS optimization algorithm can jump between different (and often non-continuous) manifolds of the redundant robot nullspace. These jumps result in an invalid trajectory. By using the configuration-

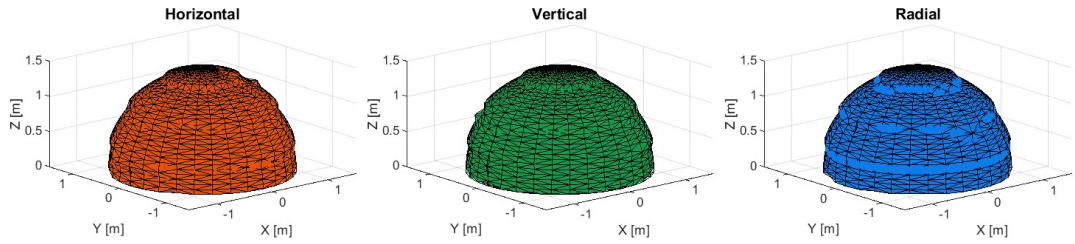

(a) Test Config 20: $k_{jl} = [0.5 \;\; 2000]$

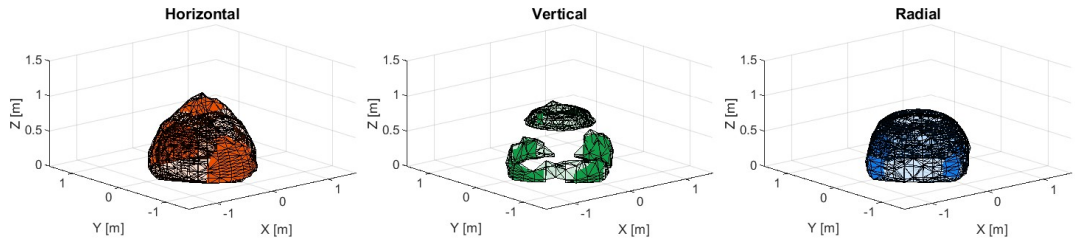

(b) Test Config 21: $k_{jl} = [50 \;\; 830]$

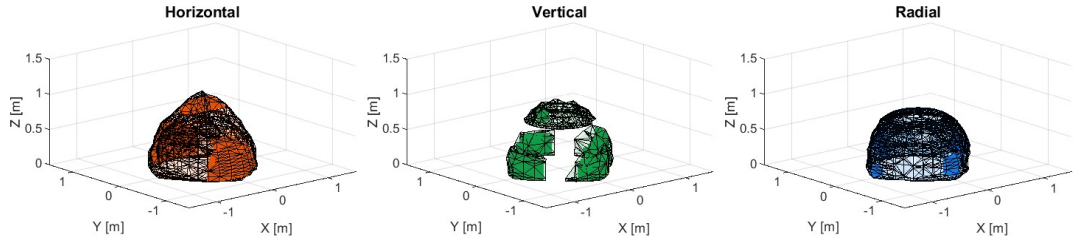

(c) Test Config 22: $k_{jl} = [50 \;\; 15000]$

Figure 5.5: STSR Regions: $k_{cd} = [120 \;\; 120 \;\; 190 \;\; 100 \;\; 100 \;\; 160]$, $\varepsilon_{psr} = 1.0$

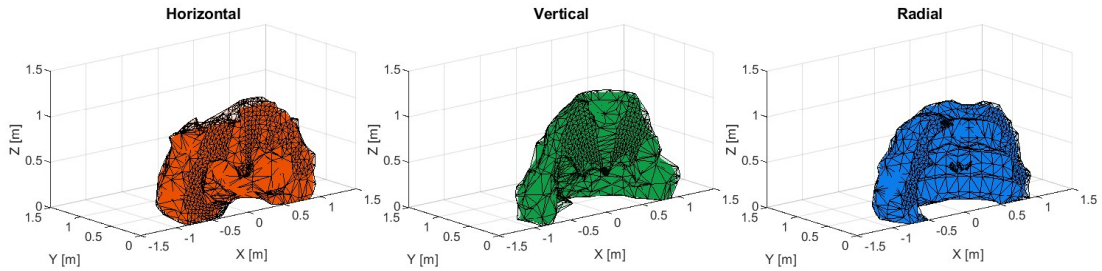

(a) Test Config 20: $k_{cd} = [120 \;\; 120 \;\; 190 \;\; 100 \;\; 100 \;\; 160]$

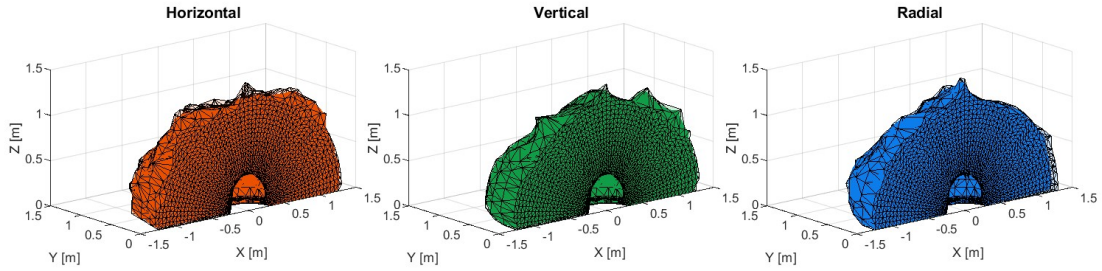

(b) Test Config 23: $k_{cd} = [120 \;\; 120 \;\; 190 \;\; 800 \;\; 500 \;\; 500]$

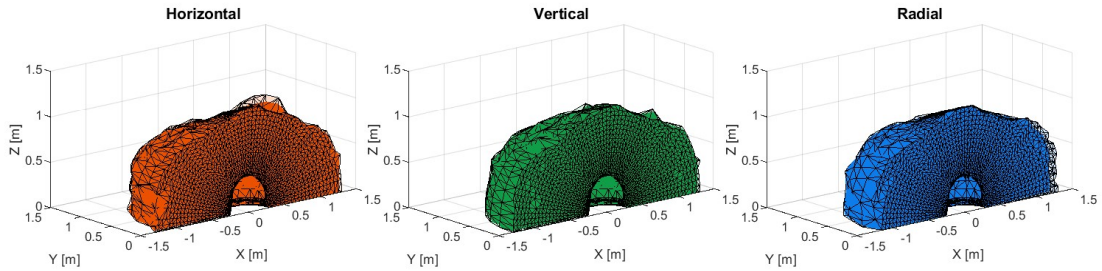

(c) Test Config 26: $k_{cd} = [120 \;\; 120 \;\; 190 \;\; 1000 \;\; 1000 \;\; 250]$

Figure 5.6: STSR Regions (XZ cross section): $k_{jl} = [50 \;\; 830]$, $\varepsilon_{psr} = 0.5$

dependent gradient descent algorithm described in subsection 2.5.2, the joint and stiffness adjuster positions can be ensured to be smooth across the task/stiffness trajectories. However, special care needs to be taken for the initial conditions of the gradient descent algorithm to ensure the trajectory starts on the optimal redundant manifold.

A method for determining this was to first generate the STSR for a given test configuration without requiring smooth STST. For each STST, the initial conditions were determined by picking a point along the trajectory closest to the centroid of the corresponding STSR. From here, the gradient descent algorithm would be initialized with 10 cold starts and then would be propagated both forward and backward along the candidate trajectory. No additional cold starts would be performed to ensure a smooth trajectory. The same process of generating alpha shapes to enclose the smooth STST would be performed to generate a series of new STSRs. As a result, these new smooth STSTs have slightly worse passive stiffness realization performance, which causes the STSR to look slightly different. However, these are all dependent on the realization threshold ε_{psr} and minimum trajectory length δ_{trj} used for the analysis.

5.3 Mechanical Joint Stiffness Limits Sensitivity Analysis

Now that a method has been developed for defining the regions of the workspace where a prescribed level of passive stiffness realization can be achieved, the sensitivity to the upper and lower mechanical joint stiffness limits can be examined. 36 different analysis configurations, varying both the desired torsional stiffness gains and mechanical joint stiffness limits, were computed for grapples in the horizontal, vertical, and radial directions. The STSR volume was then computed for a constant minimum trajectory length δ_{trj} and different realization thresholds ε_{psr}. The goal is to maximize the volume of the STSR for a given realization threshold ε_{psr}. The results were then plotted in Figure 5.7, with the desire

for the analysis configuration lines to be as far to the upper left as possible.

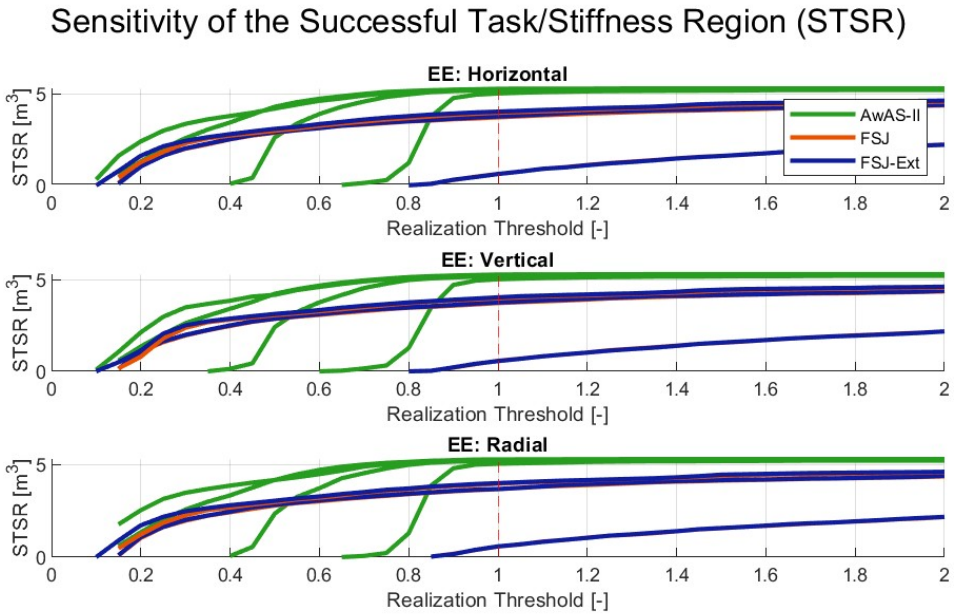

Figure 5.7: STSR Sensitivity to Mechanical Joint Stiffness Limits

From these results, a few conclusions can be made. The first is the analysis configurations with the AwAS-II joints ($k_{jl} = [0.5 \;\; 2000]$) always have a larger STSR volume when compared to the FSJ or FSJ-Extended actuators. This seems to indicate that to maximize the STSR volume, $\mathbf{k}_{jl}^{min}$ should be minimized as much as possible. Additionally, FSJ (orange) and FSJ-Extended (blue) lines lie almost exactly on top of one another. This would suggest that increasing $\mathbf{k}_{jl}^{max}$ has limited effect on the passive stiffness realization performance. The FSJ and FSJ-Extended results start to diverge as the realization threshold is lowered below $\varepsilon_{psr} \leq 0.3$. This would imply that if specific Cartesian stiffness gains were chosen so that they could be realized exactly using passive stiffness, the upper limit of the mechanical joint stiffness would start to impact the joint stiffness optimization.

It would be interesting to verify these observations by performing additional analyses lowering $\mathbf{k}_{jl}^{max}$ until the STSR volume starts to decrease. By testing the upper bound of the

mechanical joint stiffness limits, one could determine if these observations are unique to the Cartesian stiffness gains used, or would remain true for an arbitrary Cartesian stiffness matrix.

5.4 Robot Redundancy Sensitivity Analysis

All of the previous analysis uses the 7-DoF configuration of the Ranger manipulator, while the standard configuration of the Ranger manipulator has 8 degrees of freedom. This results in an extra degree of redundancy of the manipulator, which can be exploited to find a different kinematic configuration with better passive stiffness realization. By considering the 8-DoF configuration of the Ranger manipulator, one can examine how additional degrees of robot redundancy affect the passive stiffness realization performance. The results of this analysis can be seen in section 5.3.

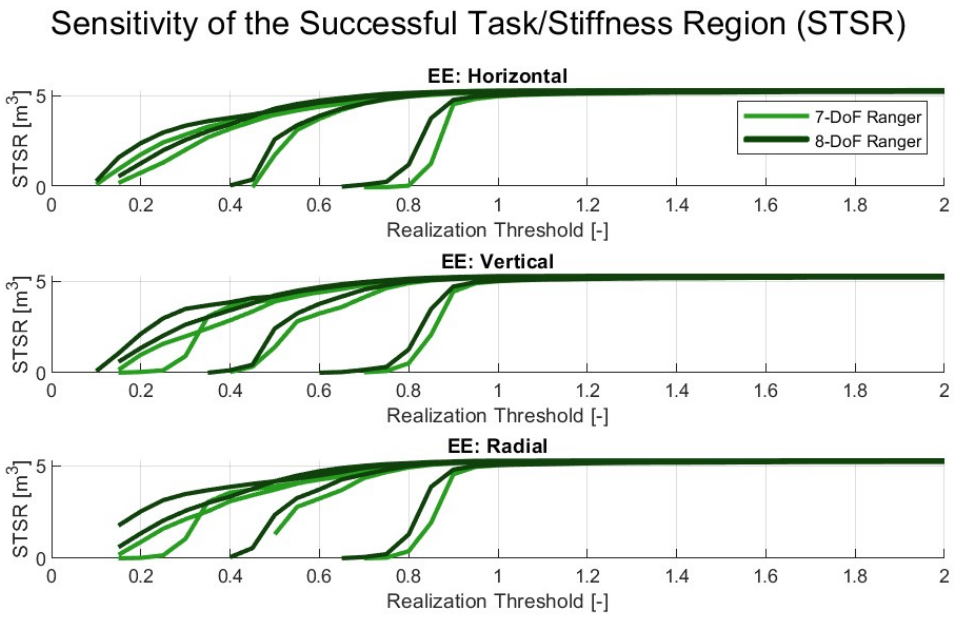

Figure 5.8: STSR Sensitivity to Degrees of Redundancy

For all three grapple trajectory directions, and different torsional stiffness gains, the 8-

DoF manipulator always had a larger STSR than the 7-DoF manipulator. Additionally, the 8-DoF manipulator was able to produce better passive stiffness realization (a lower CPJS cost function). This agrees with a 8-DoF Variable-Stiffness Robot being an under-actuated system. For it to be a fully-actuated system, there would need to be 14 degrees of freedom [1]. Thus adding additional degrees of kinematic redundancy should improve the passive stiffness realization performance.

Chapter 6: Conclusions

Variable-Stiffness Robots are commonly used for minimizing the resultant loads generated due to interactions between a manipulator and its environment. This can be traced to a Variable-Stiffness Robot's ability to implement passive stiffness to enable mechanism robustness, increase the manipulator's dynamic performance, and enable the complaint properties of the manipulator to be adapted to different tasks. These benefits are equally as desirable for the operation of Variable-Stiffness Robots on orbit. Space manipulators need to be robust to incidental contact, not inadvertently tip off the resident space object (RSO), and adapt their compliant behavior according to the inferred RSO mass and inertia. Additionally, the capability to realize a desired passive Cartesian stiffness due to the sensitivity of contact dynamics due to the absence of gravity and low damping is critical. The ability of a Variable-Stiffness Robot to provide radiation-tolerant, zero-bandwidth compliance for on-orbit servicing and active debris removal applications deserves additional research and study.

6.1 Contributions

This thesis attempted to answer two of the most critical open questions about controlling the contact dynamics using Variable-Stiffness Robots for space applications:

1. For a single, well-defined task, are there regions of the workspace where a prescribed level of passive stiffness realization can be achieved?

2. For a mobile robot (such as an on-orbit servicing satellite), can we plan trajectories within a region of the workspace to improve realization performance?

To answer these questions first, a specific satellite servicing task was defined. The robot kinematics, VSA joint limits, and desired Cartesian stiffness gains were all selected for their applicability to the specified task. This enables the results of this thesis to be directly compared to existing space manipulators using active impedance control algorithms.

Three different published passive joint stiffness optimization algorithms were introduced, and their advantages and disadvantages were examined in the context of the specific implementation within this thesis. The ability of these algorithms to generate smooth, valid trajectories was also studied. A discussion of the practicality of an online vs. offline implementation for trajectory generation was also offered.

While there has been some previous research examining the ability of a Variable-Stiffness Robot to realize an arbitrary Cartesian stiffness matrix across the entire workspace, no previous research has looked at the 3-dimensional workspace dependencies of realizing a subset of desired Cartesian stiffness matrices. The major contribution of this thesis is the development of a methodology to examine the passive stiffness workspace. Through the generation of Successful Task/Stiffness Trajectories (STST) and Successful Task/Stiffness Regions (STSR), the workspace dependencies on the passive stiffness realization can be examined for a given task. The hope is through examining the size and shape of the STSR, the design of Variable-Stiffness Robots can be both realized and optimized for a given task. A sensitivity analysis of the impacts on passive stiffness realization due to varying mechanical joint stiffness limits, additional degrees of redundancy, and different desired torsional stiffness gains was examined. For the proposed task, decreasing the mechanical joint stiffness lower bound resulted in maximizing the passive stiffness realization workspace. This can be exploited for space applications due to the ability to decrease the lower joint stiffness

limit to almost $0 Nm/rad$. This is only possible due to not needing to overcome gravitational forces. Additionally, the upper joint stiffness limit was found to have minimal effect on the volume of the STSR. As expected, increasing the manipulator's degree of redundancy improved the passive stiffness realization across the workspace. For a fully actuated Variable-Stiffness Robot, a manipulator would require 14 joints (each with a position and stiffness adjuster) to perfectly realize an arbitrary Cartesian stiffness. So, for an underactuated system, one should expect the passive stiffness realization to improve for each additional robot joint added. Future analysis would be needed to examine the trade-offs between the mechanical complexity and cost associated with adding additional degrees of redundancy for Variable-Stiffness space manipulators.

In addition to using the generation of the STSR workspace to help design the manipulator's kinematics and VSA dynamics, the inverse can also be done. Future analysis could be performed to determine the different tasks which could be performed for a given Variable-Stiffness manipulator design. Additionally, by planning trajectories to only occur within the regions where a certain level of passive stiffness realization can be ensured, the number of tasks a Variable-Stiffness Robot can execute can be expanded. In conclusion, the methods developed in this thesis enable the verification of the design and performance of a Variable-Stiffness Robot to grapple RSO.

6.2 Final Remarks and Future Work

While significant advancements were made in assessing the workspace where a Variable-Stiffness Robot can successfully grapple an RSO, a few simplifying assumptions were needed due to a lack of published literature. One such simplification was the relation between a realized Cartesian stiffness matrix and the success of a grapple. The foundational paper describing RSO contact dynamics [19] only listed a single set of acceptable Carte-

sian stiffness gains. As a result, it was impossible to infer the sensitivity of realizing these gains for ensuring a successful grapple. This thesis got around this issue by using a single normalized realization threshold ε_{psr} to determine whether the Cartesian stiffness behavior was acceptable. However, one could imagine that the contact dynamics could be more sensitive to specific gains. Ideally, a series of contact dynamics simulations would be performed to understand this relation, and modifications to the optimization cost function or weighting matrix could be performed to provide better pass/fail grapple criteria.

Additionally, while the present analysis is sufficient for initial passive stiffness workspace analysis, additional fidelity of the internal VSA dynamics is needed. This thesis ignores most of the internal dynamics within a VSA except for the mechanical joint stiffness limits. As a result, trajectories are defined at the link $(\mathbf{q})$ and joint stiffness $(\mathbf{k}_j)$ space. However, there exist additional limitations internal to the VSA which could result in invalid trajectories. For example, the position and stiffness adjuster motors both have a maximum velocity and torque which can be applied. The trajectories in this thesis assume that both motors can react instantaneously to produce the desired trajectory. As a result, to ensure that Successful Task/Stiffness Trajectories are feasible, future analysis should include the increased fidelity model.

While not considered in this thesis, another major research area that needs to be thoroughly investigated prior to employing Variable-Stiffness Robots on orbit is the effect of the absence of gravity on the manipulator equilibrium convergence. For terrestrial Variable-Stiffness Robots, the deflection of the VSA elastic element is dominated by gravitational forces. This results in a robot converging to a predictable, deflected equilibrium configuration (i.e. absolute stability). On orbit, due to the lack of excitation of the elastic element, the highly stochastic joint friction can result in only marginal stability of the VSA joint position. This unique feature of the on-orbit environment requires the development of new control algorithms that can provide robust control of the marginally stable system.

In conclusion, this thesis has developed a series of methods and analysis techniques for examining the performance of Variable-Stiffness Robots for grappling RSO. While most current research has been directed toward their use for terrestrial human-robot interaction applications, Variable-Stiffness Robots might be even better suited for the space environment. The ability to instantaneously react to changes in the robot's environment is highly attractive for a situation with limited computational power, significant control time delays, low inherent damping, and zero gravity. While more research is required, the author believes that implementing passive stiffness into space manipulators could greatly improve their ability to perform the necessary on-orbit servicing, assembly, and debris removal tasks of the future.

Appendix A: Test Matrix and Additional Results

While only a small subset of results was discussed in chapter 5, the Task/Stiffness Workspace analysis was performed on 40 different test configurations. These test configurations were created by varying the desired Cartesian stiffness gains, upper and lower joint stiffness, optimization algorithm, and the number of degrees of redundancy. The test configuration matrix can be found in Table A.1. Additionally, the STSR volumes for four different passive stiffness mapping thresholds are reported in Table A.2.

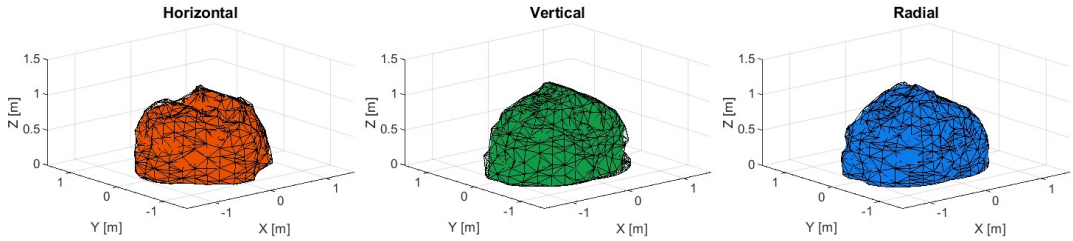

(a) Test Config 23: $k_{jl} = [0.5 \;\; 2000]$

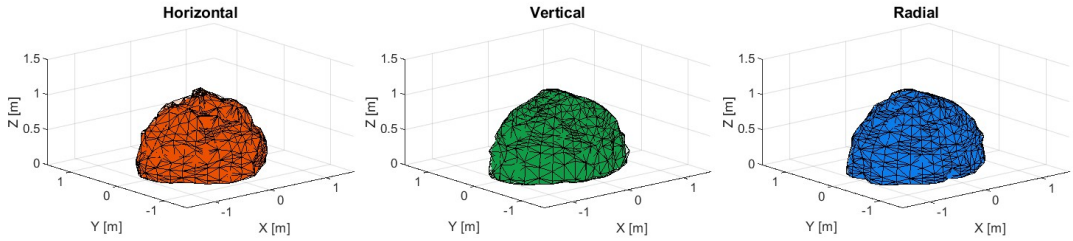

(b) Test Config 24: $k_{jl} = [50 \;\; 830]$

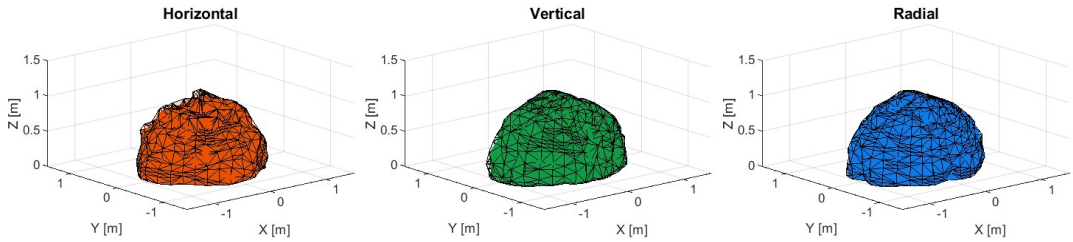

(c) Test Config 25: $k_{jl} = [50 \;\; 15000]$

Figure A.1: STSR Regions: $k_{cd} = [120 \;\; 120 \;\; 190 \;\; 800 \;\; 500 \;\; 500]$, $\varepsilon_{psr} = 0.3$

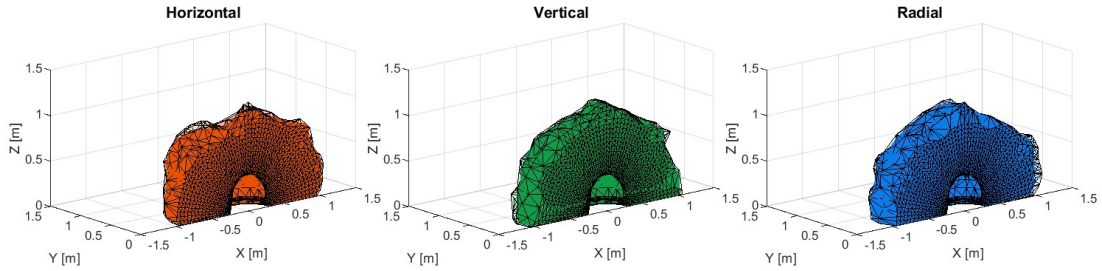

(a) Test Config 23: $k_{jl} = [0.5 \;\; 2000]$

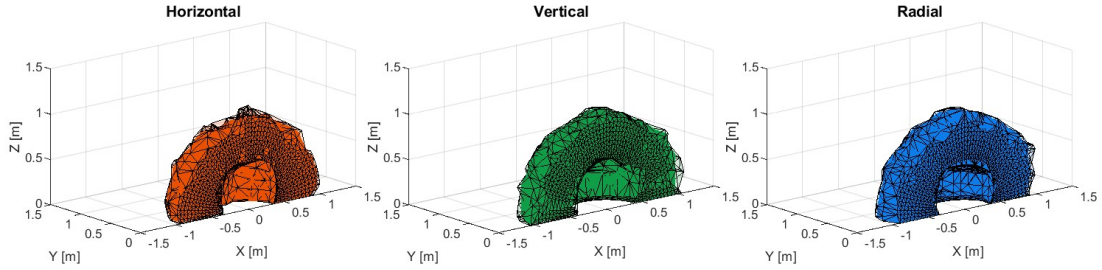

(b) Test Config 24: $k_{jl} = [50 \;\; 830]$

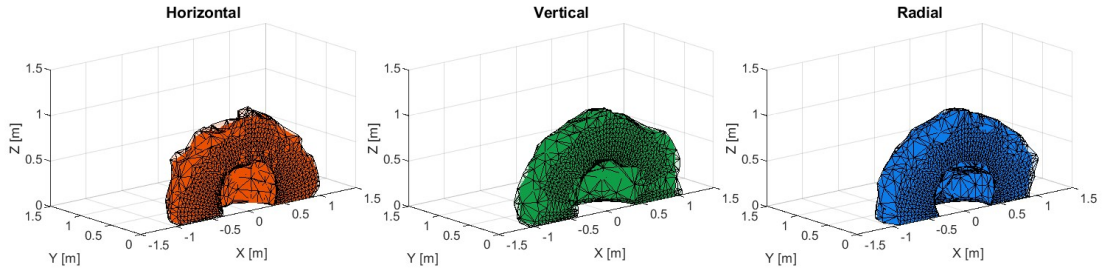

(c) Test Config 25: $k_{jl} = [50 \;\; 15000]$

Figure A.2: STSR Regions (XZ cross section): $k_{cd} = [120 \;\; 120 \;\; 190 \;\; 800 \;\; 500 \;\; 500]$, $\varepsilon_{psr} = 0.3$

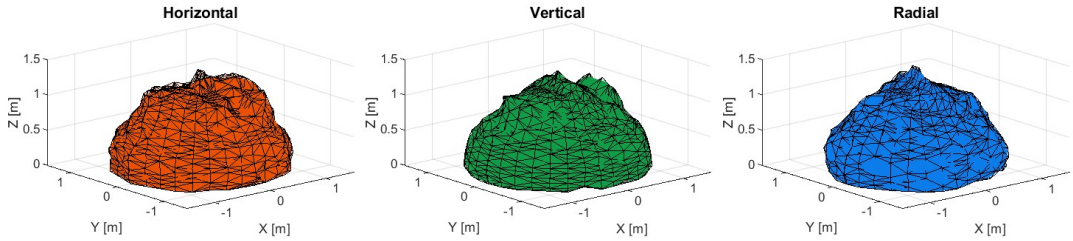

(a) Test Config 23: $k_{jl} = [0.5 \;\; 2000]$

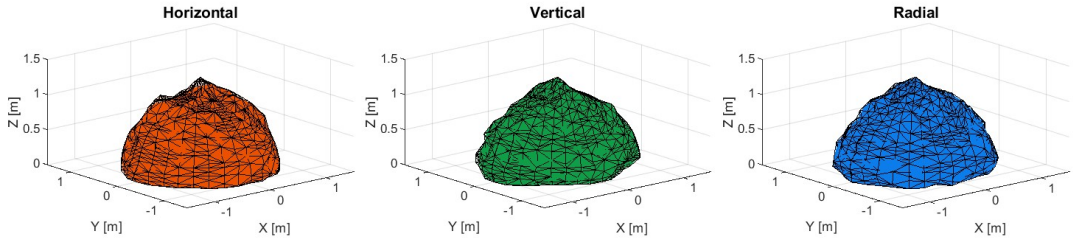

(b) Test Config 24: $k_{jl} = [50 \;\; 830]$

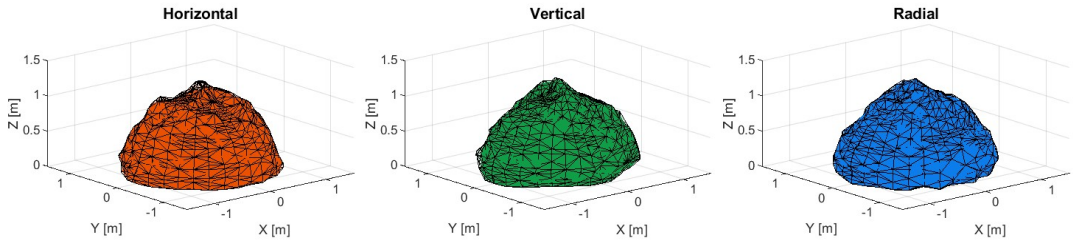

(c) Test Config 25: $k_{jl} = [50 \;\; 15000]$

Figure A.3: STSR Regions: $k_{cd} = [120 \;\; 120 \;\; 190 \;\; 800 \;\; 500 \;\; 500]$, $\varepsilon_{psr} = 0.5$

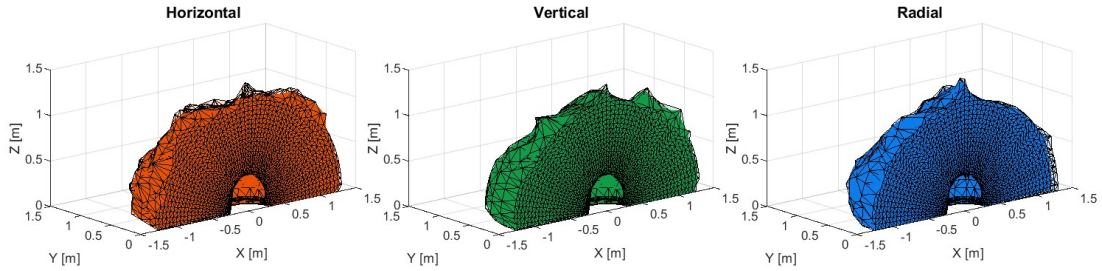

(a) Test Config 23: $k_{jl} = [0.5 \;\; 2000]$

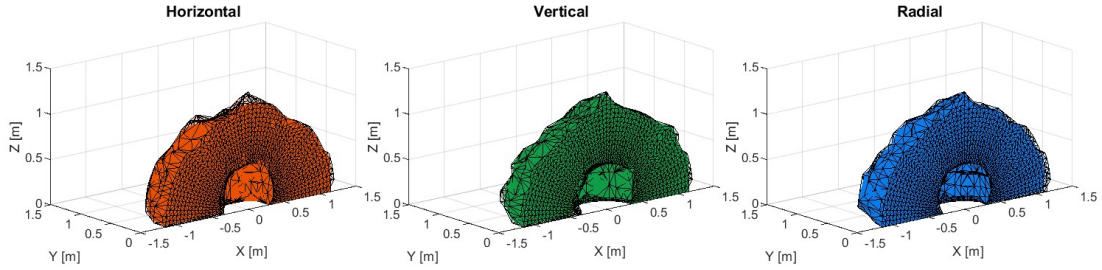

(b) Test Config 24: $k_{jl} = [50 \;\; 830]$

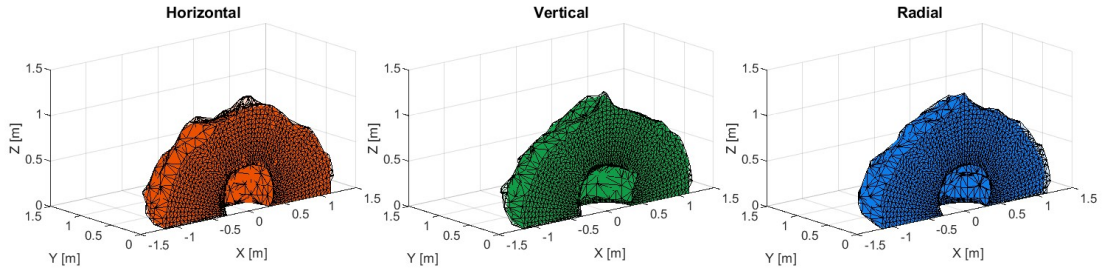

(c) Test Config 25: $k_{jl} = [50 \;\; 15000]$

Figure A.4: STSR Regions (XZ cross section): $k_{cd} = [120 \;\; 120 \;\; 190 \;\; 800 \;\; 500 \;\; 500]$, $\varepsilon_{psr} = 0.5$

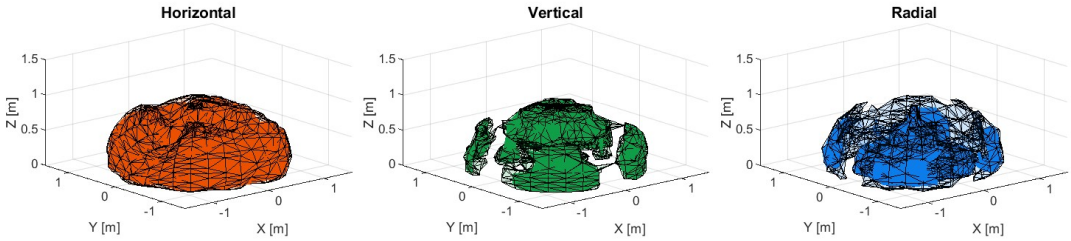

(a) Test Config 26: $k_{jl} = [0.5 \;\; 2000]$

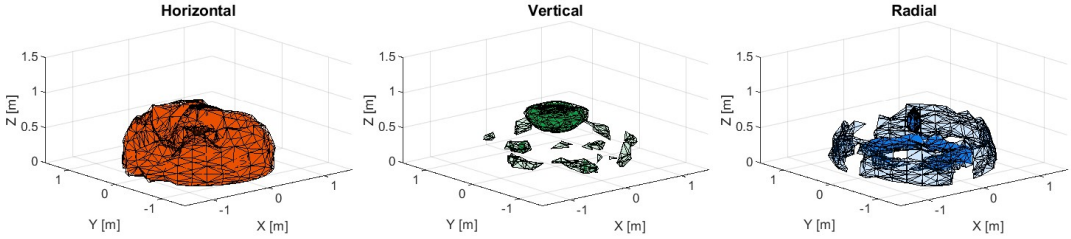

(b) Test Config 27: $k_{jl} = [50 \;\; 830]$

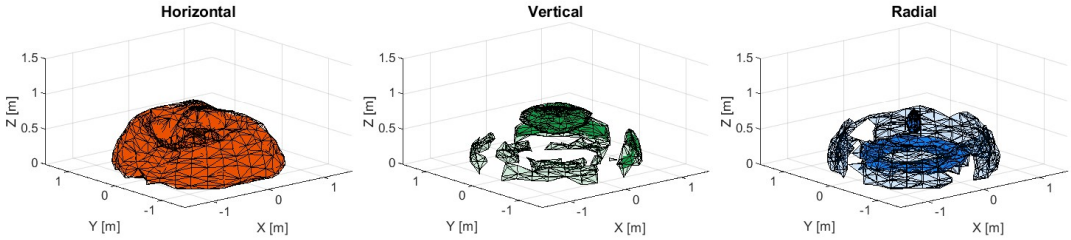

(c) Test Config 28: $k_{jl} = [50 \;\; 15000]$

Figure A.5: STSR Regions: $k_{cd} = [120 \;\; 120 \;\; 190 \;\; 1000 \;\; 1000 \;\; 250]$, $\varepsilon_{psr} = 0.3$

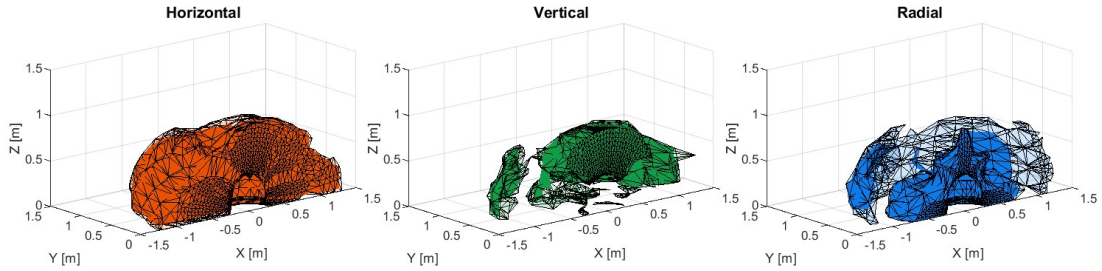

(a) Test Config 26: $k_{jl} = [0.5 \;\; 2000]$

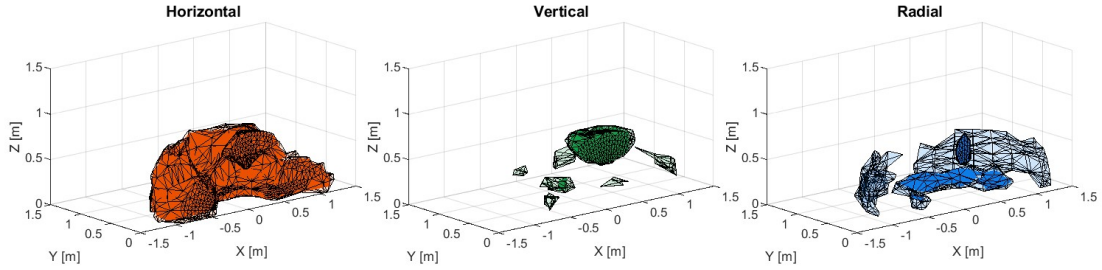

(b) Test Config 27: $k_{jl} = [50 \;\; 830]$

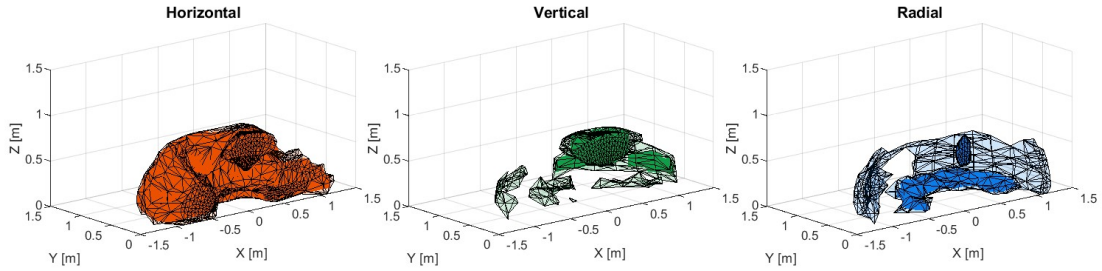

(c) Test Config 28: $k_{jl} = [50 \;\; 15000]$

Figure A.6: STSR Regions (XZ cross section): $k_{cd} = [120 \;\; 120 \;\; 190 \;\; 1000 \;\; 1000 \;\; 250]$, $\varepsilon_{psr} = 0.3$

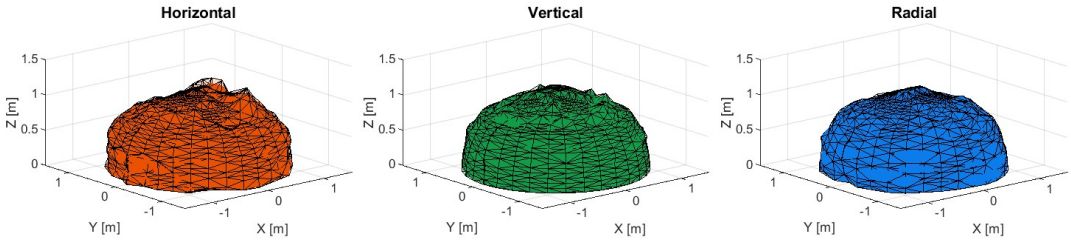

(a) Test Config 26: $k_{jl} = [0.5 \;\; 2000]$

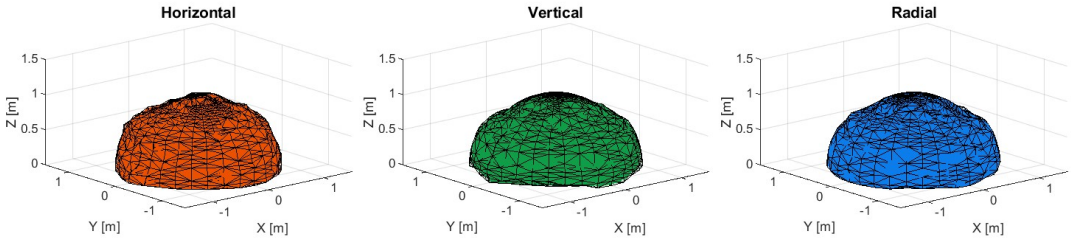

(b) Test Config 27: $k_{jl} = [50 \;\; 830]$

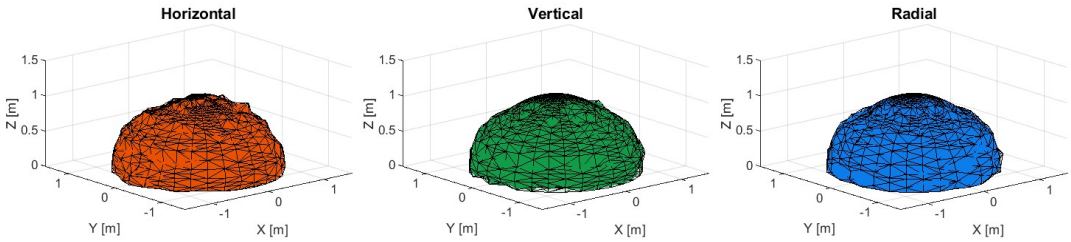

(c) Test Config 28: $k_{jl} = [50 \;\; 15000]$

Figure A.7: STSR Regions: $k_{cd} = [120 \;\; 120 \;\; 190 \;\; 1000 \;\; 1000 \;\; 250]$, $\varepsilon_{psr} = 0.5$

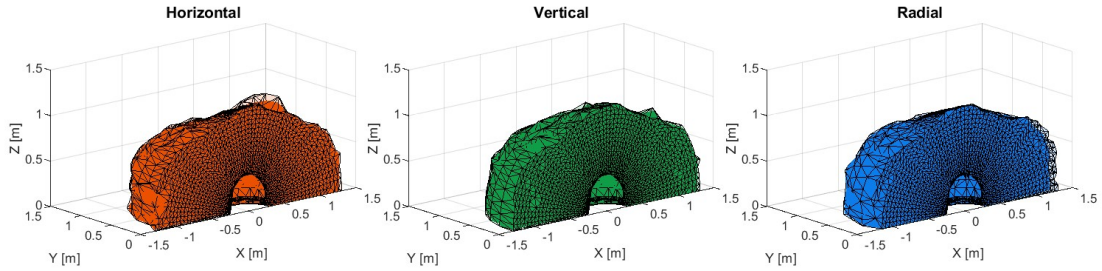

(a) Test Config 26: $k_{jl} = [0.5 \;\; 2000]$

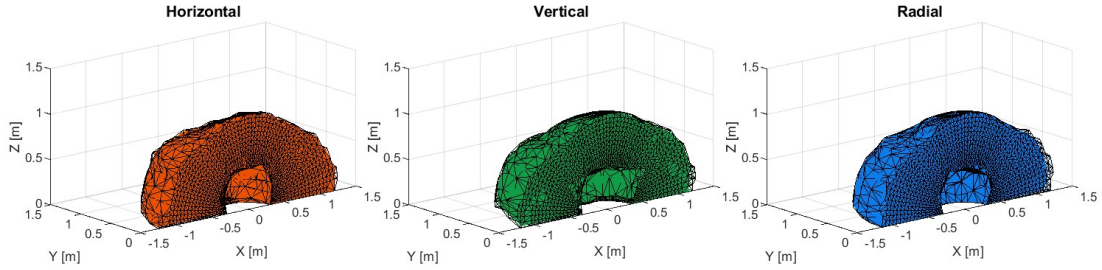

(b) Test Config 27: $k_{jl} = [50 \;\; 830]$

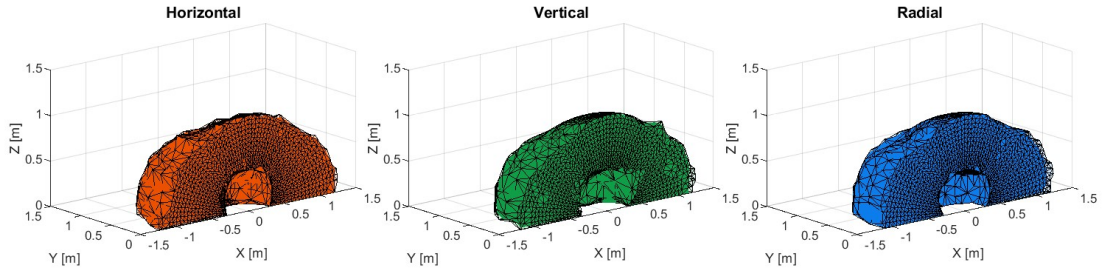

(c) Test Config 28: $k_{jl} = [50 \;\; 15000]$

Figure A.8: STSR Regions (XZ cross section): $k_{cd} = [120 \;\; 120 \;\; 190 \;\; 1000 \;\; 1000 \;\; 250]$, $\varepsilon_{psr} = 0.5$

Table A.1: STSR Test Matrix

#	Desired Cartesian Stiffness Gain	k_{jl}^{min}	k_{jl}^{max}	Algorithm	DoF
1	[120, 120, 190, 25, 25, 40]	0.5	2000	CPJC	7
2	[120, 120, 190, 25, 25, 40]	50	830	CPJC	7
3	[120, 120, 190, 25, 25, 40]	50	1500	CPJC	7
4	[120, 120, 190, 25, 25, 40]	50	15000	CPJC	7
5	[120, 120, 190, 100, 100 160]	0.5	2000	CPJC	7
6	[120, 120, 190, 100, 100 160]	50	830	CPJC	7
7	[120, 120, 190, 100, 100 160]	50	1500	CPJC	7
8	[120, 120, 190, 100, 100 160]	50	15000	CPJC	7
9	[120, 120, 190, 800, 500, 500]	0.5	2000	CPJC	7
10	[120, 120, 190, 800, 500, 500]	50	830	CPJC	7
11	[120, 120, 190, 800, 500, 500]	50	1500	CPJC	7
12	[120, 120, 190, 800, 500, 500]	50	15000	CPJC	7
13	[120, 120, 190, 1000, 1000, 250]	0.5	2000	CPJC	7
14	[120, 120, 190, 1000, 1000, 250]	50	830	CPJC	7
15	[120, 120, 190, 1000, 1000, 250]	50	1500	CPJC	7
16	[120, 120, 190, 1000, 1000, 250]	50	15000	CPJC	7
17	[120, 120, 190, 25, 25, 40]	0.5	2000	CPJS	7
18	[120, 120, 190, 25, 25, 40]	50	830	CPJS	7
19	[120, 120, 190, 25, 25, 40]	50	15000	CPJS	7
20	[120, 120, 190, 100, 100 160]	0.5	2000	CPJS	7
21	[120, 120, 190, 100, 100 160]	50	830	CPJS	7
22	[120, 120, 190, 100, 100 160]	50	15000	CPJS	7
23	[120, 120, 190, 800, 500, 500]	0.5	2000	CPJS	7
24	[120, 120, 190, 800, 500, 500]	50	830	CPJS	7
25	[120, 120, 190, 800, 500, 500]	50	15000	CPJS	7
26	[120, 120, 190, 1000, 1000, 250]	0.5	2000	CPJS	7
27	[120, 120, 190, 1000, 1000, 250]	50	830	CPJS	7
28	[120, 120, 190, 1000, 1000, 250]	50	15000	CPJS	7
29	[120, 120, 190, 25, 25, 40]	0.5	2000	CPJS	8
30	[120, 120, 190, 25, 25, 40]	50	830	CPJS	8
31	[120, 120, 190, 25, 25, 40]	50	15000	CPJS	8
32	[120, 120, 190, 100, 100 160]	0.5	2000	CPJS	8
33	[120, 120, 190, 100, 100 160]	50	830	CPJS	8
34	[120, 120, 190, 100, 100 160]	50	15000	CPJS	8
35	[120, 120, 190, 800, 500, 500]	0.5	2000	CPJS	8
36	[120, 120, 190, 800, 500, 500]	50	830	CPJS	8
37	[120, 120, 190, 800, 500, 500]	50	15000	CPJS	8
38	[120, 120, 190, 1000, 1000, 250]	0.5	2000	CPJS	8
39	[120, 120, 190, 1000, 1000, 250]	50	830	CPJS	8
40	[120, 120, 190, 1000, 1000, 250]	50	15000	CPJS	8

Table A.2: STSR Volume vs. Realization Threshold

Test Number	Direction	**STSR Volume** (m^3)				
#	-	$\varepsilon_{psr} = 0.3$	$\varepsilon_{psr} = 0.5$	$\varepsilon_{psr} = 1.0$	$\varepsilon_{psr} = 1.5$	$\varepsilon_{psr} = 2.0$
17	Horz	-	-	4.96	5.17	5.21
17	Vert	-	-	5.00	5.17	5.21
17	Rad	-	-	5.03	5.17	5.21
18	Horz	-	-	-	-	-
18	Vert	-	-	-	-	-
18	Rad	-	-	-	-	-
19	Horz	-	-	-	-	-
19	Vert	-	-	-	-	-
19	Rad	-	-	-	-	-
20	Horz	-	1.76	5.17	5.22	5.25
20	Vert	-	1.40	5.18	5.22	5.25
20	Rad	-	1.30	5.18	5.21	5.24
21	Horz	-	-	0.42	1.40	2.01
21	Vert	-	-	0.12	1.22	1.88
21	Rad	-	-	0.22	1.41	2.04
22	Horz	-	-	0.41	1.41	1.99
22	Vert	-	-	0.12	1.24	1.88
22	Rad	-	-	0.22	1.41	2.04
23	Horz	2.04	3.96	5.27	5.29	5.29
23	Vert	1.98	3.89	5.25	5.28	5.28
23	Rad	2.11	3.71	5.25	5.28	5.29
24	Horz	1.56	2.63	3.56	4.03	4.29
24	Vert	1.54	2.52	3.56	4.08	4.36
24	Rad	1.63	2.64	3.68	4.16	4.38
25	Horz	1.56	2.66	3.63	4.06	4.34
25	Vert	1.56	2.51	3.58	4.09	4.37
25	Rad	1.63	2.65	3.70	4.17	4.38
26	Horz	2.87	3.94	5.27	5.29	5.30
26	Vert	0.91	4.02	5.26	5.28	5.29
26	Rad	1.05	3.90	5.26	5.28	5.29
27	Horz	1.53	2.80	3.87	4.29	4.51
27	Vert	0.16	2.91	3.86	4.39	4.53
27	Rad	0.25	2.90	3.96	4.40	4.61
28	Horz	1.72	2.91	3.96	4.39	4.58
28	Vert	0.22	2.98	3.87	4.45	4.59
28	Rad	0.01	2.92	3.98	4.43	4.62

Bibliography

[1] Alin Albu-Schaffer, Oliver Eiberger, Markus Grebenstein, Sami Haddadin, Christian Ott, Thomas Wimböck, Sebastian Wolf, and Gerd Hirzinger. Soft robotics. *Robotics & Automation Magazine, IEEE*, 15:20–30, 2008.

[2] Alin Albu-Schaffer, Markus Fischer, G. Schreiber, F. Schoeppe, and Gerd Hirzinger. Soft robotics: what cartesian stiffness can obtain with passively compliant, uncoupled joints? In *2004 IEEE/RSJ International Conference on Intelligent Robots and Systems (IROS) (IEEE Cat. No.04CH37566)*, volume 4, pages 3295–3301 vol.4, 2004.

[3] Alin Albu-Schaffer and Gerd Hirzinger. Cartesian impedance control techniques for torque controlled light-weight robots. In *Proceedings 2002 IEEE International Conference on Robotics and Automation (Cat. No.02CH37292)*, volume 1, pages 657–663 vol.1, 2002.

[4] Alin Albu-Schäffer, S. Wolf, O. Eiberger, S. Haddadin, F. Petit, and M. Chalon. Dynamic modelling and control of variable stiffness actuators. In *2010 IEEE International Conference on Robotics and Automation*, pages 2155–2162, 2010. ISSN: 1050-4729.

[5] Alex Ellery. Tutorial review on space manipulators for space debris mitigation. *Robotics*, 8(2):34, 2019.

[6] Alin Albu-Schaffer and Antonio Bicchi. Actuators for soft robotics. In *Springer Handbook of Robotics*, pages 499–530. Springer, 2nd edition, 2016.

[7] Craig R. Carignan and Russell D. Howard. A partitioned redundancy management scheme for an eight-joint revolute manipulator. *Journal of Robotic Systems*, 17(9):453–468, 2000. _eprint: https://onlinelibrary.wiley.com/doi/pdf/10.1002/1097-4563%28200009%2917%3A9%3C453%3A%3AAID-ROB1%3E3.0.CO%3B2-A.

[8] Christian Ott. *Cartesian Impedance Control of Redundant and Flexible-Joint Robots*, volume 49 of *Springer Tracts in Advanced Robotics*. Springer, 2008. ISSN: 1610-7438, 1610-742X.

[9] Thomas Debus and Sean Dougherty. Overview and performance of the front-end robotics enabling near-term demonstration (FREND) robotic arm. In *AIAA Infotech@Aerospace Conference*, Infotech@Aerospace Conferences. American Institute of Aeronautics and Astronautics, 2009.

[10] M.A. Diftler, J.S. Mehling, M.E. Abdallah, N.A. Radford, L.B. Bridgwater, A.M. Sanders, R.S. Askew, D.M. Linn, J.D. Yamokoski, F.A. Permenter, B.K. Hargrave, R. Platt, R.T. Savely, and R.O. Ambrose. Robonaut 2 - the first humanoid robot in space. In *2011 IEEE International Conference on Robotics and Automation*, pages 2178–2183, 2011. ISSN: 1050-4729.

[11] Evangelos Papadopoulos, Farhad Aghili, Ou Ma, and Roberto Lampariello. Robotic manipulation and capture in space: A survey. *Frontiers in Robotics and AI*, 8, 2021.

[12] Cliff Fitzgerald. Developing baxter. In *2013 IEEE Conference on Technologies for Practical Robot Applications (TePRA)*, pages 1–6, 2013. ISSN: 2325-0534.

[13] Florian Patrick Petit. *Analysis and Control of Variable Stiffness Robots*. phdthesis, ETH Zurich, 2014.

[14] Werner Friedl, Hannes Höppner, Florian Petit, and Gerd Hirzinger. Wrist and forearm rotation of the DLR hand arm system: Mechanical design, shape analysis and experimental validation. In *2011 IEEE/RSJ International Conference on Intelligent Robots and Systems*, pages 1836–1842, 2011. ISSN: 2153-0866.

[15] Markus Grebenstein, Alin Albu-Schäffer, Thomas Bahls, Maxime Chalon, Oliver Eiberger, Werner Friedl, Robin Gruber, Sami Haddadin, Ulrich Hagn, Robert Haslinger, Hannes Höppner, Stefan Jörg, Mathias Nickl, Alexander Nothhelfer, Florian Petit, Josef Reill, Nikolaus Seitz, Thomas Wimböck, Sebastian Wolf, Tilo Wüsthoff, and Gerd Hirzinger. The DLR hand arm system. In *2011 IEEE International Conference on Robotics and Automation*, pages 3175–3182, 2011. ISSN: 1050-4729.

[16] Giorgio Grioli, Sebastian Wolf, Manolo Garabini, Manuel Catalano, Etienne Burdet, Darwin Caldwell, Raffaella Carloni, Werner Friedl, Markus Grebenstein, Matteo Laffranchi, et al. Variable stiffness actuators: The user's point of view. *The International Journal of Robotics Research*, 34(6):727–743, 2015.

[17] Stefan S. Groothuis, Giacomo Rusticelli, Andrea Zucchelli, Stefano Stramigioli, and Raffaella Carloni. The variable stiffness actuator vsaUT-II: Mechanical design, modeling, and identification. *IEEE/ASME Transactions on Mechatronics*, 19(2):589–597, 2014.

[18] Yisheng Guan and Kazuhito Yokoi. Reachable space generation of a humanoid robot using the monte carlo method. In *2006 IEEE/RSJ International Conference on Intelligent Robots and Systems*, pages 1984–1989, 2006. ISSN: 2153-0866.

[19] Carl Henshaw and Frederick Tasker. Managing contact dynamics for orbital robotic servicing missions. In *AIAA SPACE 2008 Conference & Exposition*, AIAA SPACE Forum. American Institute of Aeronautics and Astronautics, 2008.

[20] Carl Glen Henshaw, Samantha Glassner, Bo Naasz, and Brian Roberts. Grappling spacecraft. *Annual Review of Control, Robotics, and Autonomous Systems*, 5(1):137–159, 2022. _eprint: https://doi.org/10.1146/annurev-control-042920-011106.

[21] Neville Hogan. Mechanical impedance of single- and multi-articular systems. In Jack M. Winters and Savio L-Y. Woo, editors, *Multiple Muscle Systems: Biomechanics and Movement Organization*, pages 149–164. Springer, 1990.

[22] Amir Jafari, Nikos Tsagarakis, and Darwin Caldwell. A novel intrinsically energy efficient actuator with adjustable stiffness (AwAS). *Mechatronics, IEEE/ASME Transactions on*, 18:355–365, 2013.

[23] Jorge Angeles and Frank C. Park. Design and performance evaluation. In *Springer Handbook of Robotics*, pages 399–418. Springer, 2 edition, 2016.

[24] Manuel Keppler, Dominic Lakatos, Christian Ott, and Alin Albu-Schaffer. Elastic structure preserving (ESP) control for compliantly actuated robots. *IEEE Transactions on Robotics*, PP:1–19, 2018.

[25] Luigi Villani and Joris De Schutter. Force control. In *Springer Handbook of Robotics*, pages 195–220. Springer, 2nd edition, 2016.

[26] J.S. Mehling, M.A. Diftler, M. Chu, and M. Valvo. A minimally invasive tendril robot for in-space inspection. In *The First IEEE/RAS-EMBS International Conference on Biomedical Robotics and Biomechatronics, 2006. BioRob 2006.*, pages 690–695, 2006. ISSN: 2155-1782.

[27] Hiroki Nakanishi, Masaaki Kodama, and Kazuya Yoshida. Influence of control time delay on the dynamics of satellite capture. *TRANSACTIONS OF THE JAPAN SOCIETY FOR AERONAUTICAL AND SPACE SCIENCES, SPACE TECHNOLOGY JAPAN*, 7:Pf_29–Pf_34, 2009.

[28] Andrew Ogilvie, Justin Allport, Michael Hannah, and John Lymer. Autonomous satellite servicing using the orbital express demonstration manipulator system. In *Proc. of the 9th International Symposium on Artificial Intelligence, Robotics and Automation in Space (i-SAIRAS'08)*, pages 25–29, 2008.

[29] Florian Petit and Alin Albu-Schäffer. Cartesian impedance control for a variable stiffness robot arm. In *2011 IEEE/RSJ International Conference on Intelligent Robots and Systems*, pages 4180–4186, 2011. ISSN: 2153-0866.

[30] G.A. Pratt and M.M. Williamson. Series elastic actuators. In *Proceedings 1995 IEEE/RSJ International Conference on Intelligent Robots and Systems. Human Robot Interaction and Cooperative Robots*, volume 1, pages 399–406 vol.1, 1995.

[31] Jacob J. Rice and Joseph M. Schimmels. Passive compliance control of redundant serial manipulators. *Journal of Mechanisms and Robotics*, 10(4), 2018.

[32] S. Roderick, B. Roberts, E. Atkins, and D. Akin. The ranger robotic satellite servicer and its autonomous software-based safety system. *IEEE Intelligent Systems*, 19(5):12–19, 2004. Conference Name: IEEE Intelligent Systems.

[33] Enrico Sabelli. Categorizing admittance control parameters for the ranger 8-dof teleoperated space manipulator. mastersthesis, University of Maryland, College Park, 2007.

[34] E. B. Saff and A. B. J. Kuijlaars. Distributing many points on a sphere. *The Mathematical Intelligencer*, 19(1):5–11, 1997.

[35] J. Kenneth Salisbury. Active stiffness control of a manipulator in cartesian coordinates. In *1980 19th IEEE Conference on Decision and Control including the Symposium on Adaptive Processes*, pages 95–100, 1980.

[36] Minghe Shan, Jian Guo, and Eberhard Gill. Review and comparison of active space debris capturing and removal methods. *Progress in Aerospace Sciences*, 80:18–32, 2016.

[37] Stefano Chiaverini, Giuseppe Oriolo, and Anthony A. Maciejewski. Redundant robots. In *Springer Handbook of Robotics*, pages 221–242. Springer, 2nd edition, 2016.

[38] G. Tonietti, R. Schiavi, and A. Bicchi. Design and control of a variable stiffness actuator for safe and fast physical human/robot interaction. In *Proceedings of the 2005 IEEE International Conference on Robotics and Automation*, pages 526–531, 2005. ISSN: 1050-4729.

[39] B. Vanderborght, A. Albu-Schaeffer, A. Bicchi, E. Burdet, D. G. Caldwell, R. Carloni, M. Catalano, O. Eiberger, W. Friedl, G. Ganesh, M. Garabini, M. Grebenstein, G. Grioli, S. Haddadin, H. Hoppner, A. Jafari, M. Laffranchi, D. Lefeber, F. Petit, S. Stramigioli, N. Tsagarakis, M. Van Damme, R. Van Ham, L. C. Visser, and S. Wolf. Variable impedance actuators: A review. *Robotics and Autonomous Systems*, 61(12):1601–1614, 2013.

[40] Sebastian Wolf, Oliver Eiberger, and Gerd Hirzinger. The DLR FSJ: Energy based design of a variable stiffness joint. In *2011 IEEE International Conference on Robotics and Automation*, pages 5082–5089, 2011. ISSN: 1050-4729.

[41] Sebastian Wolf and Jan-Emmo Feenders. Modeling and benchmarking energy efficiency of variable stiffness actuators on the example of the DLR FSJ. In *2016 IEEE/RSJ International Conference on Intelligent Robots and Systems (IROS)*, pages 529–536, 2016. ISSN: 2153-0866.

[42] Sebastian Wolf, Giorgio Grioli, Oliver Eiberger, Werner Friedl, Markus Grebenstein, Hannes Höppner, Etienne Burdet, Darwin G. Caldwell, Raffaella Carloni, Manuel G. Catalano, Dirk Lefeber, Stefano Stramigioli, Nikos Tsagarakis, Michaël Van Damme, Ronald Van Ham, Bram Vanderborght, Ludo C. Visser, Antonio Bicchi, and Alin Albu-Schäffer. Variable stiffness actuators: Review on design and components. *IEEE/ASME Transactions on Mechatronics*, 21(5):2418–2430, 2016. Conference Name: IEEE/ASME Transactions on Mechatronics.

[43] Franziska Zacharias, Christoph Borst, and Gerd Hirzinger. Capturing robot workspace structure: representing robot capabilities. In *2007 IEEE/RSJ International Conference on Intelligent Robots and Systems*, pages 3229–3236, 2007. ISSN: 2153-0866.